frontiers | Frontiers in Earth Science

TYPE Original Research
PUBLISHED 11 September 2025
DOI 10.3389/feart.2025.1601135

OPEN ACCESS

EDITED BY
J. Gregory Shellnutt,
National Taiwan Normal University, Taiwan

REVIEWED BY
Basilios Tsikouras,
Universiti Brunei Darussalam, Brunei
Muhammad Saleem Mughal,
University of Azad Jammu and Kashmir, Pakistan

*CORRESPONDENCE
Bowen Zhang,
54392171@qq.com

RECEIVED 27 March 2025
ACCEPTED 18 August 2025
PUBLISHED 11 September 2025

CITATION
Sun Y, Zhang B, Yao Y, Zhan X, Yalikun Y and Wang Y (2025) Magma mixing in the Karamaili granite belt of Eastern Junggar: evidence from A2-type granites and their mafic microgranular enclaves.
Front. Earth Sci. 13:1601135.
doi: 10.3389/feart.2025.1601135

Magma mixing in the Karamaili granite belt of Eastern Junggar: evidence from A2-type granites and their mafic microgranular enclaves

Yafei Sun[1,2], Bowen Zhang[3]*, Yuan Yao[1,2], Xinzhong Zhan[3], Yaxiaer Yalikun[3] and Yacong Wang[3]

[1]Xinjiang Pamir Intracontinental Subduction National Observation and Research Station, Beijing, China, [2]Urumqi Institute of Central Asia Earthquake, China Earthquake Administration, Urumqi, China, [3]Xinjiang Key Laboratory for Geodynamic Processes and Metallogenic Prognosis of the Central Asian Orogenic Belt, College of Geology and Mining Engineering, Xinjiang University, Urumqi, China

The Karamaili Orogenic Belt forms an essential part of the southernmost margin of the Eastern Junggar Orogenic Belt. The Late Carboniferous granitic belt of the Karamaili belt provides a valuable natural setting for studying the evolution of silicic magmas. In this study the petrology, rock geochemistry, and chronology of granite and mafic microgranular enclaves (MMEs) in the Sabei, Huangyangshan, and Sujiquan plutons are investigated. The results show similar zircon U-Pb ages of 315.9 ± 2.4 Ma, 316.1 ± 2.2 Ma, 319.4 ± 2.0 Ma, and 313.9 ± 3.5 Ma for the granite and Sabei MMEs. The granites are high silica, alkali-rich, weakly alkaline to sub-aluminous A_2-type, and are strongly depleted in Eu. They are enriched in Ta, Th, U, Rb, K, and Pb, and formed in a post-collisional extensional environment. In contrast, the Sabei MMEs are sub-aluminous, calc-alkaline to high-K calc-alkaline gabbroic enclaves that exhibit typical magmatic structures and evidence of mixing and evolution. They represent residual dioritic enclaves derived from underplated, rising mafic magma that underwent mixing. Whole-rock εNd(t) values of +4.0 to +4.5 for the Sabei, Huangyangshan, and Sujiquan plutons, and εNd(t) values of +5.5 to +5.7 for the Sabei MMEs, indicate the involvement of juvenile mantle-derived magmas, suggesting significant juvenile crustal growth in the region. The results reveal intense mafic magmatism associated with the Karamaili granites. It included mafic magma input that generated highly differentiated granites, such as the Kamusite granite and mafic magmatic components contributing to eastern plutons and forming alkaline granites rich in dioritic enclaves like the Sabei and Huangyangshan granites. This study provides petrogenetic constraints on the formation of plutons in the Karamaili Granite Belt and the evolution of siliceous magmas in the region.

KEYWORDS

Eastern Junggar, Karamaili granitic belt, A-type granite, mafic microgranular enclaves, magma mixing

1 Introduction

Magma mixing, a key intrusion mechanism in igneous rock-forming systems, is crucial in understanding petrogenetic processes and analyzing magma evolution, crust-mantle interactions, and magmatic dynamics. (Hoskin and Ireland, 2000; Li, 2002; Barbarin, 2005; Kumar and Rino, 2006; Słaby and Martin, 2008). Granitic rocks that host mafic microgranular enclaves (MMEs) provide valuable insights into crust-mantle interactions by acting as a "lithoprobe" and "window" from which direct evidence of magma mixing can be obtained and a pathway to investigate the deep lithosphere (Barbarin and Didier, 1992). Barbarin (1988) introduced the term MMEs to describe mafic rocks enclosed within other magmatic rocks. MMEs typically have a darker color than surrounding rocks (Barbarin, 2005), such as calc-alkaline granites. Magmatic mixing is ubiquitous and occurs not only in I-type granites but also in S-type and A-type granites (Wang, 2000; Bonin, 2007; Shellnutt et al., 2010; Champion and Bultitude, 2013).

The Central Asian Orogenic Belt (CAOB) is the largest accretionary orogenic belt and continental crust growth zone that has formed since the Phanerozoic era. The complete process of the ancient Asian Ocean generation, subduction, closure, and collision-related development is preserved within its rocks (Sengör and Natal'in, 1996; Xiao et al., 2008; Xiao and Santosh, 2014). The Junggar structural belt is typically divided into three main components: the Western Junggar Orogenic Belt, the Junggar Basin, and the Eastern Junggar Orogenic Belt (EJOB) (Figure 1b). The latter is located in the southwestern part of the CAOB (Figure 1a) and consists of a series of Paleozoic magmatic arcs and accretionary complexes that have recorded the formation and evolution of the ancient Asian Ocean (Xiao et al., 2010; Xiao and Santosh, 2014). Intense crust-mantle interactions occur in this area during the continental margin accretionary orogeny and post-collisional vertical crustal growth (Xiao et al., 2008). The Paleozoic tectonic evolution in this region was critical to the growth of continental crust and the evolution of the ancient Asian Ocean. Establishing and refining the complete magmatic evolution in this area thus plays a vital role in reconstructing the ancient tectonic framework of northern Xinjiang and understanding the evolutionary history of the CAOB (Xiao et al., 2019b). The Karamaili tectonic belt is located in the EJOB north of the Karamaili Fault (Figure 1c), and represents the inferred termination point of the Paleozoic oceanic basin in the Junggar region (Li et al., 2012). However, the magmatic source region, tectonic setting, and evolutionary history of this area have consistently been points of contention in basic geological research of the Karamaili region (Su et al., 2007; Tang et al., 2007; Su et al., 2008; Yang et al., 2008; Zhang et al., 2013; Liu et al., 2017; Zhang et al., 2018; Zhang et al., 2020; Wang et al., 2021).

The Karamaili Granite Belt (KGB) comprises A-type granites, as evidenced by positive εNd(t) and εHf(t) values. These granite types are corroborated by the presence of mafic-ultramafic plutons, including active late-stage vein plutons, which indicate Late Paleozoic magmatic activity (Hong et al., 1995; Han et al., 1997). Nevertheless, significant spatial disparities have emerged concerning the petrography, degree of magmatic fractionation, mafic magma supply, and magma mixing in the area. A study of the late Silurian to early Devonian Karamaili serpentinite belt (Xu et al., 2014) proposed the development of a local extensional tectonic setting during the late stages of ancient oceanic plate subduction in the region, which led to substantial silicic magma activity. Mantle-derived material was the reason for the growth of the ancient lithospheric crust and the formation of the juvenile crust. Although this model is widely accepted (Wang and Hou, 2018), uncertainties regarding the diversity of granites due to crust-mantle magma mixing remain, and a comprehensive analysis of the evolution of magma mixing in a crystal mush state is lacking (Mo, 2011; Kröner et al., 2017; Wang, 2017). Thus, this study focuses on the eastern segment of the KGB, in which numerous MMEs have been observed in the Sabei, Huangyangshan, and Sujiquan plutons. This study is based on previous investigations and utilizes additional petrography and geochemical data, zircon U-Pb dating, and whole-rock Nd isotope analysis of the granites and their MMEs to determine the origin of magma mixing and magma evolution to provide insights into different evolutionary processes during the Late Carboniferous in this granitic belt and the transition from compressional to extensional stress environments in the late subduction stages.

2 Geological background

The Karamaili tectonic belt is located on the eastern edge of the Junggar Block in Xinjiang, with its tectonic structure lying at the junction between the Siberian Plate and the Kazakhstan-Junggar Block. The eastern margin of the Junggar Block has undergone long-term and complex tectonic evolution since the Paleozoic era, accompanied by intense magmatic activity, forming of the WNW-oriented Karamaili ophiolite belt and the parallel KGB in the southeastern part of the block. The Karamaili structural belt is currently primarily controlled by the Karamaili, Ulungu, and Erqisi deep faults. The region is also affected by a series of WNW-striking strike-slip faults associated with tectonic activity and the occurrence of A-type granites.

The Karamaili tectonic belt is an important part of the Paleozoic orogenic belt in Eastern Junggar. A northwest-striking ophiolite belt, potentially containing Early Devonian oceanic crust, occurs discontinuously along the northern flank of the Karamaili deep fault (Li, 1995). The exposed strata in the area are mainly Devonian and Carboniferous tuffaceous siltstone and pyroclastic rocks, with a small fraction of Silurian strata scattered to the south. The NW-trending Late Carboniferous KGB developed in this area, with rock types predominantly plagiogranite, granodiorite, biotite granite, hornblende granite and alkaline granite. Calc-alkaline granites associated with gold and copper metallogenic series and alkali-rich or highly differentiated granites related to the tin metallogenic series are the most significant (Yang et al., 2009; Gu et al., 2020). The KGB outcrop is a roughly NW-oriented, banded, massive batholith extending approximately 110 km in length and covering an area of approximately 1,068 km^2. Previous authors have divided the belt into the Kamusite, Laoyaquan, Belekuduke, Sabei, Huangyangshan, and Sujiquan plutons from west to east. The plutons are generally considered an A-type granite series with a magmatic age of approximately 330–310 Ma (Su et al., 2008; Yang et al., 2008; Zhang et al., 2018) indicating that the KGB entered a post-collision extensional tectonic environment in the Late Carboniferous.

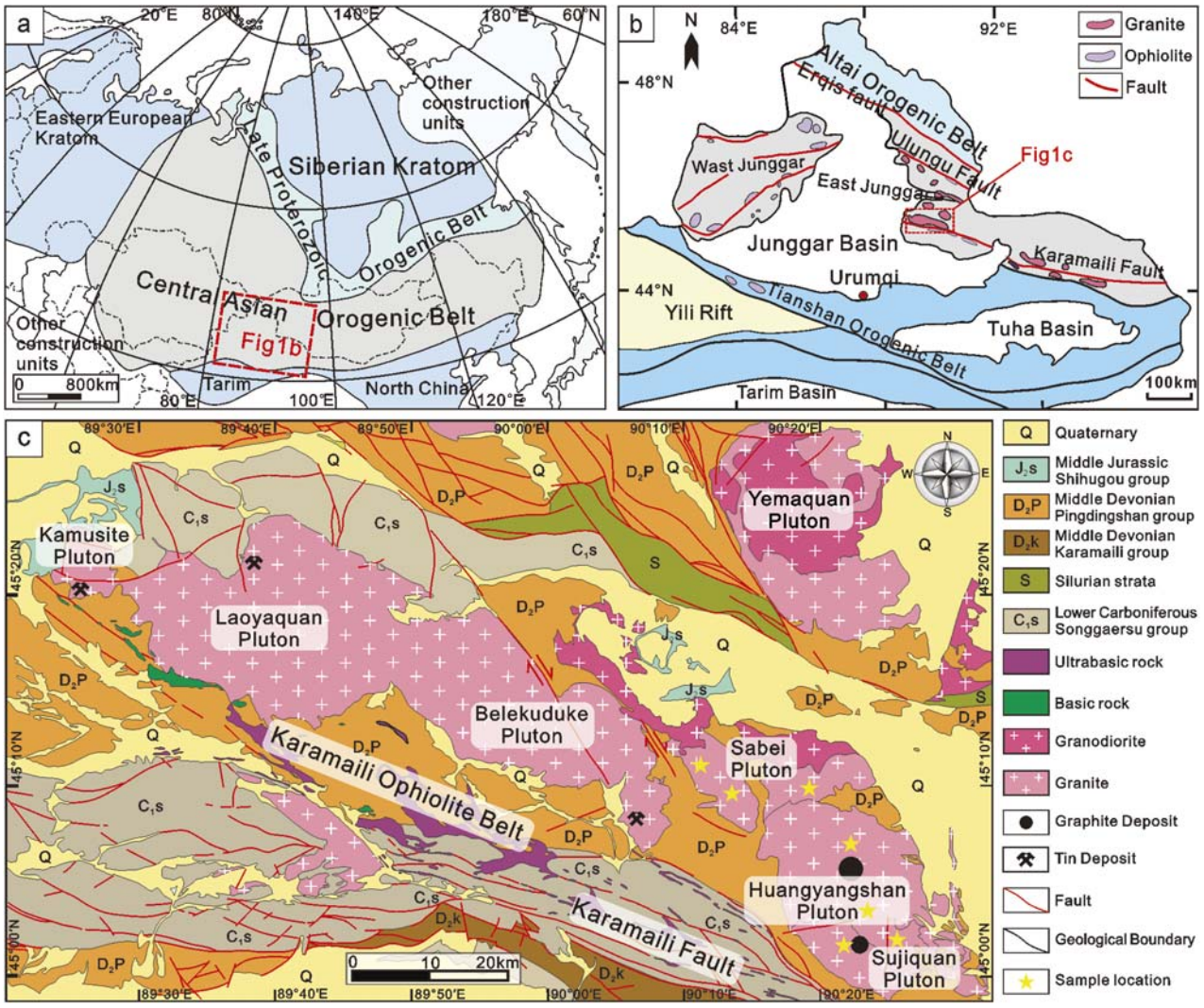

FIGURE 1
(a) Simplified geologic map of the Central Asian Orogenic Belt, modified from Xiao et al. (2019a); **(b)** Regional tectonic map of northern Xinjiang, modified from Chen and Jahn (2004); **(c)** Geological map of the Karamaili belt.

This study focuses on the Sabei, Huangyangshan, and Sujiquan plutons in the eastern KGB, which are rich in MMEs and exhibit significant spatial variations in terms of petrology, the degree of magma differentiation, mafic magma input, and magma mixing effects (Figure 1c). The Sabei pluton comprises coarse- to medium-grained biotite granite and medium- to fine-grained potassic granite; it is in contact with the overlying Middle Devonian and Quaternary strata. A change in lithology occurs to the north of this pluton, and granodiorite is present (Figure 1c). The Huangyangshan pluton is located on the northeastern side of the fracture zone (Figure 1c). It is a spherical weathered outcrop with an exposure area of approximately 230 km^2. It has intrusive relations with the tuffaceous siltstone of the Carboniferous Heishantou Formation. Thermal metamorphism occurs at the contact with the wall rock to varying degrees. The local grain size becomes finer close to the contact area. Graphite mineralization developed simultaneously in both plutons and occurred as a series of NE-trending granite porphyry veins, diorite veins, and a small number of diabase veins. The Sujiquan pluton is mainly composed of plagioclase granite, granodiorite, biotite granite, and alkali feldspar granite. The biotite granite is closely related to tin mineralization. Mesothermal graphite deposits are commonly found in the rock bodies, and the overlying strata are primarily Devonian and Carboniferous siltstone and pyroclastic rock (Liu et al., 1997; Lin et al., 2007; Lin et al., 2008).

3 Petrography

According to field observations and thin-section microscopic analysis, the lithology of the sample includes monzogranite, biotite syenogranite, biotite granite, and MMEs, which are shown in Figure 2a.

The monzogranite is mainly distributed in the Sabei pluton, with fresh surfaces generally appearing gray-white and having blocky structures. The pluton comprises medium- to coarse-grained

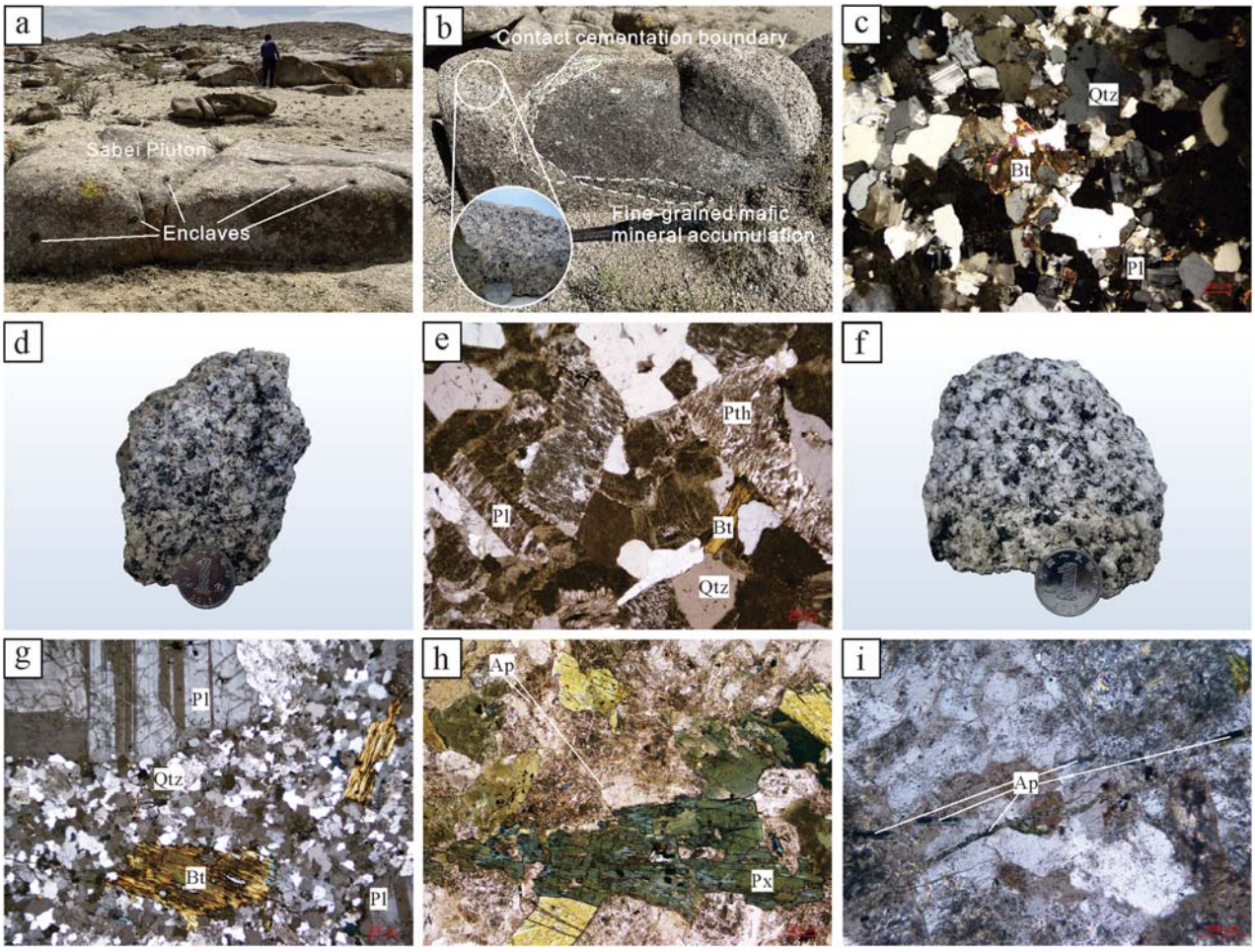

FIGURE 2
Field photographs and micrographs of **(a)** the Sabei granites and mafic microgranular enclaves (MMEs); **(b,c)** Sabei alkaline feldspar granite; **(d,e)** Huangyangshan biotite potassium feldspar granite; **(f,g)** Sujiquan biotite granite; **(h)** Sabei MMEs. **(i)** Needle-like apatite in Sabei MMEs (Pl, Plagioclase; Pth, Perthite; Bt, Biotite; Qtz, Quartz; Ap, Apatite; Px, Pyroxene.

monzogranite (Figure 2b) composed of alkali feldspar (35%–40%), plagioclase (30%–35%), quartz (25%–30%), and accessory biotite (3%–5%). The alkali feldspar is heterogeneous with a grain size of 0.2–4 mm, and striped feldspar is predominant (Figure 2c), with the stripes fusiform in the exsolution direction and displaying weak kaolinization. Plagioclase occurs as subhedral grains displaying polysynthetic twinning (Albite law) and pervasive sericitization with argillic alteration. Quartz is anhedral with a grain size ranging from 0.5 to 5.5 mm, but generally greater than 3 mm.

The biotite syenogranite is primarily distributed in the Huangyangshan pluton, with a medium to fine-grained, subhedral, and massive structure. The main minerals are potassium feldspar (60%–65%), quartz (20%–25%), biotite (5%–10%) and plagioclase (<5%) (Figure 2d). The alkali feldspar is well-formed and has a grain size of 0.4–4 mm; it is generally about 2 mm. Potassium feldspar has undergone kaolinization. Quartz is anhedral (0.5–3.5 mm), displaying homogeneous extinction and no evidence of secondary alteration (e.g., sericitization or chloritization) along the grain margins (Figure 2e). Plagioclase exsolution lamellae are evident comprising mainly albite; these grains are subhedral and exhibit polysynthetic twinning (Albite law) and weak sericitization. Biotite occurs as subhedral flakes (grain size 0.2–1 mm), exhibiting light brown pleochroism. It has been partially altered to chlorite and iron oxides along cleavage planes.

The biotite granite is mainly distributed in the Sujiquan plutons, with a gray-white fresh surface, a medium- and coarse-grained texture and blocky structures (Figure 2f). It is composed of potassium feldspar (40%–45%), plagioclase (30%–35%), quartz (20%–25%), and a small amount of biotite (8%–10%). Alkali feldspar is euhedral to subhedral (grain size 0.2–4.5 mm) predominantly orthoclase with minor kaolinization (Figure 2g). Plagioclase (albite) displays Carlsbad twin law with sharp twin boundaries, suggesting magmatic crystallization, while biotite occurs as brown subhedral flakes (0.4–2 mm) associated with accessory zircon and apatite.

The MMEs in the granite of the Sabei and Huangyangshan plutons are spherical, ellipsoidal, spindle-shaped, and lenticular, although the majority are ellipsoidal. The size of the long axis in the enclaves varies significantly, ranging from a few meters to a few millimeters. The MMEs are grey-black, contrasting sharply with the host rocks' color. The MMEs exhibits a fine-grained,

subhedral granular massive texture, marked by chilled margins and concentrations of fine-grained mafic minerals (Figure 2b). Its main minerals are plagioclase (30%–35%), biotite (25%–30%), alkali feldspar (10%–15%), pyroxene (10%–15%), hornblende (5%–10%), quartz (5%–10%), and more typical needle-like apatite (Figures 2h,i). Plagioclase occurs predominantly as euhedral tabular crystals exhibiting oscillatory zoning, indicating it resulted from magma mixing (Xie et al., 2004).

4 Analytical methods

Fourteen fresh granite samples were collected from undeformed and unaltered bedrock outcrops without late vein penetration in the Sabei, Huangyangshan, and Sujiquan plutons. The samples' whole-rock geochemical composition was determined. Zircon U-Pb dating was performed on samples SB-1, HYS-1, SJQ-1, and SBMMEs-1, whereas whole-rock Nd isotope analysis was conducted on samples SB-1, SB-3, SBMME-1, SBMME-3, HYS-1, and SJQ-2. The samples comprised four pieces of medium-grained monzogranite from the Sabei pluton (SBMME-1 to SBMME-3), three pieces of MMEs from the medium-grained monzogranite in Sabei (SBMME-1 to SBMME-3), four pieces of biotite syenogranite from Huangyangshan (HYS-1 to HYS-4), and four pieces of biotite granite from the Sujiquan pluton (SJQ-1 to SJQ-4).

4.1 Zircon U-Pb geochronology

Zircon crushing, single mineral selection, target development, and U-Pb and cathodoluminescence (CL) image acquisition were performed at Beijing Yanduzhongshi Geological Analysis Laboratories, Ltd. Zircon U-Pb dating was performed using a laser ablation system with a UP-213 deep ultraviolet laser (213 nm), and a MicroLas optical system. Inductively coupled plasma mass spectrometry (ICP-MS) was performed using a Jena M90, with the international zircon standard 91500. The ordinary Pb calibration method was used to calibrate the measurement results. ICP-MS DataCal software was used for data processing (Liu et al., 2010). Zircon U-Pb concordia diagrams and the mean squared weighted deviation (MSWD) were obtained using Isoplot. The age value error of 1σ was used in determining the $^{206}Pb/^{238}U$ age, and a 95% confidence interval was utilized (Ludwig, 2003).

4.2 Whole-rock geochemistry

Whole-rock geochemical analysis was performed at the Beijing Yanduzhongshi Geological Analysis Laboratories, Ltd. Fourteen fresh samples (none of the materials showed were altered) were ultrasonically cleaned with deionized water, oven-dried at 60 °C for 24 h, and pulverized to <75 μm using an agate mortar prior to geochemical analysis. For the whole rock major element testing, the sample powder was weighed and mixed with lithium tetraborate ($Li_2B_4O_7$) as a flux in a ratio of 1:8. Ammonium nitrate (NH_4NO_3) was added as an oxidant, and lithium bromide (LiBr) was added as a flux. The sample was heated to 1,050 °C for 15 min using a fusion furnace to form a uniform glass sheet in a platinum crucible. Testing was conducted using wavelength dispersive X-ray fluorescence (XRF) (Zetium, Malvern PANalytical, Malvern, United Kingdom), with a relative standard deviation (RSD) of less than 2%. The sample powder was weighed, placed in a polytetrafluoroethylene dissolution tank, and HF + HNO_3 was added prior to whole-rock trace element analysis. The material was placed in a high-pressure digestion tank in a drying oven at 190 °C for 72 h, after which it was removed for acid flushing. The solution was diluted to a constant volume for machine testing. Testing was completed using the Agilent 7700 ICP-MS, and a testing accuracy of better than 10% was achieved.

4.3 Whole-rock Nd isotopic composition analyses

Nd isotope analysis was performed using six sets of whole-rock samples at Beijing Yanduzhongshi Geological Analysis Laboratories Ltd. First, 0.25 g of the sample was accurately weighed and placed into a Teflon stew tank. HNO_3 and HF were added, and the sample was heated for 48 h digestion under closed conditions at 190 °C. The temperature was reduced to 160 °C under closed conditions to remove any HF. The HNO_3 solution was added, and the mixture was dissolved at a temperature of 150 °C over 6 h under sealed conditions until a constant volume of 25 g was achieved. An appropriate amount of the Nd solution was centrifuged. The obtained suspension supernatant was evaporated to dryness, and the solution was adjusted to a suitable pH. A special LN resin was used to separate the pure Nd and obtain a sample solution. Finally, multi-collector ICP-MS (MC-ICP-MS) (Neptune Plus, Thermo Fisher Scientific) was performed to determine the $^{143}Nd/^{144}Nd$ value for the sample solution. According to the exponential law for $^{143}Nd/^{144}Nd$ (0.7218), online mass fractionation correction was performed on the measured $^{143}Nd/^{144}Nd$ values with an error of 2σ (uncertainty in the mass spectrometry measurement).

5 Results

5.1 Zircon geochronology

Laser ablation-ICP-MS (LA-ICP-MS) zircon U-Pb dating was performed on three granite samples and one enclave sample from the Sabei, Huangyangshan, and Sujiquan plutons in the eastern KGB. Rectangular zircons with a complete crystal structure were selected under transmitted and reflected light, and CL images were obtained to perform zircon U-Pb dating (Figure 3). The data used for zircon U-Pb dating are presented in Table 1.

5.1.1 Zircon geochronology of granites

The zircons in the monzogranite, biotite syenogranite, and biotite granite samples are subhedral to euhedral, predominantly showing elongated prismatic morphology with well-developed bipyramidal terminations (120–230 μm), with aspect ratios ranging from 1.5:1 to 3:1. Clear oscillatory bands and nucleation rims are observed in the CL images of the zircons (Figures 3a–c); these zones have Th/U values higher than 0.1 indicating distinct magmatic characteristics (Hoskin and Ireland, 2000; Belousova et al., 2002).

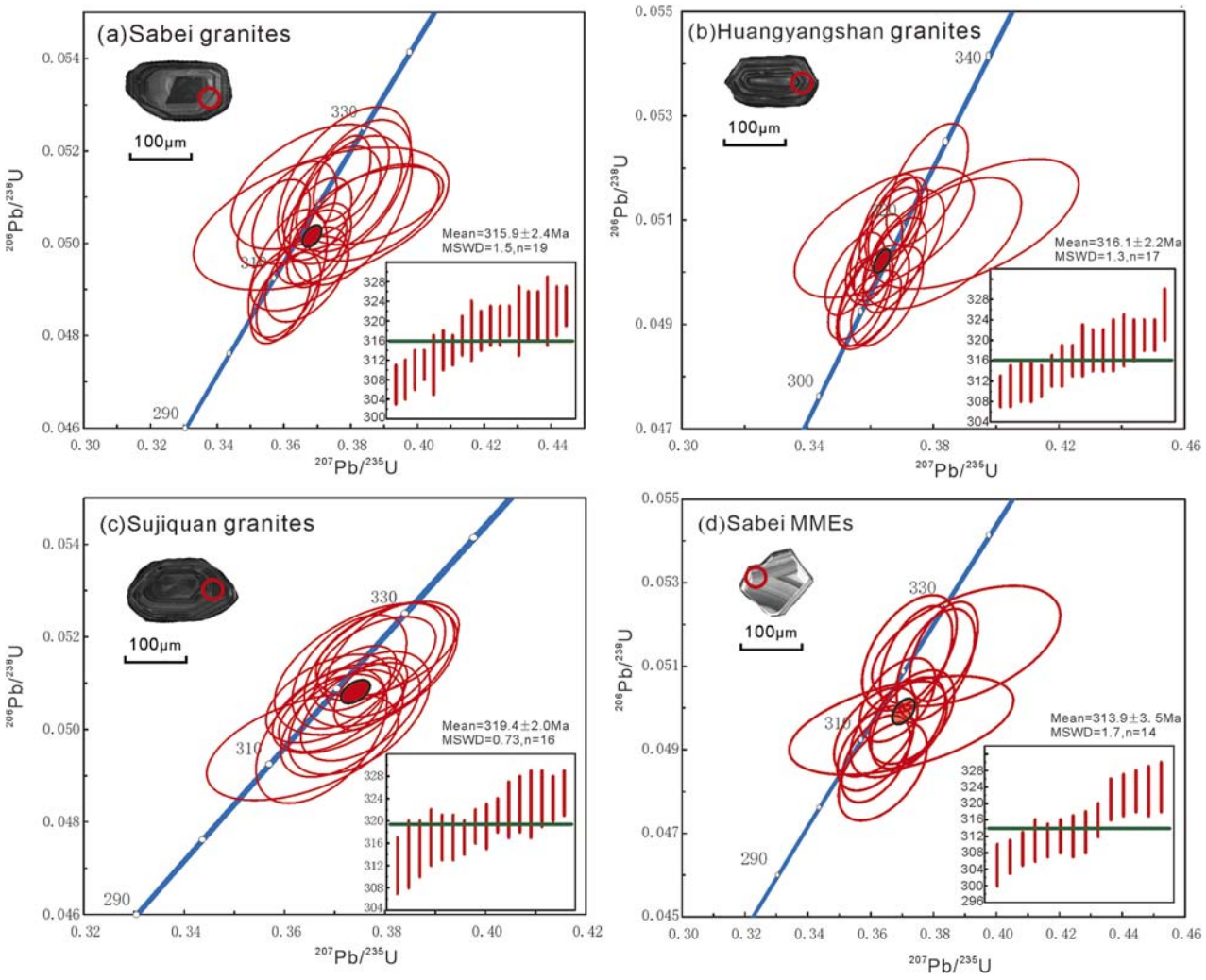

FIGURE 3
Zircon U–Pb Concordia diagrams, weighted average age map, and zircon CL image of the **(a)** Sabei granites, **(b)** Huangyangshan granites, **(c)** Sujiquan granite, and **(d)** Sabei MMEs.

The dates obtained from the zircons of the plutons are less than 1,000 Ma, therefore, the $^{206}Pb/^{238}U$ dates are adopted.

Analysis of 19 spots in sample SB1 from the Sabei pluton shows Th and U contents of zircons ranging from 79.26–318.50 ppm to 177.27–734.71 ppm, respectively. The Th/U ratio of the zircons ranges from 0.38 to 0.59 indicating a magmatic origin of the zircon. The test points on the samples fall predominantly on or near the Concordia, with the degree of concordance greater than 95%. The weighted average $^{206}Pb/^{238}U$ age of 315.9 ± 2.4 Ma (MSWD = 1.3, $n = 17$) (Figure 3a) indicates a Late Carboniferous crystallization age for the monzogranite.

Analysis of 17 spots from zircons in sample HYS1 from the Huangyangshan pluton shows significant variation in the Th and U contents of the zircons, with values of 42.59–766.04 ppm and 117.92–850.62 ppm, respectively, and a Th/U ratio ranging from 0.33 to 0.90, suggesting a magmatic origin of the zircons. The age concordance of the 17 test points is within the 95% confidence interval, and the weighted average $^{206}Pb/^{238}U$ age is 316.1 ± 2.2 Ma (MSWD = 1.3, $n = 17$) (Figure 3b), indicating a Late Carboniferous crystallization age for the biotite syenogranite.

Analysis of 16 target points in sample SJQ1 from the Sujiquan rock mass shows Th and U contents of 30.80–554.01 ppm and 77.59–1095.79 ppm, respectively, with Th/U ratios of 0.34–0.51, indicating a magmatic origin of the zircon. The analysis point has a consistent concordant age, and its $^{206}Pb/^{238}U$ weighted average age is 319.4 ± 2.0 Ma (MSWD = 0.73, $n = 16$) (Figure 3c), also indicating a Late Carboniferous crystallization age for the biotite granite.

5.1.2 Zircon geochronology of MMEs

The zircons in the MMEs of the Sabei pluton are subhedral prismatic crystals. They are colorless and transparent, with bipyramidal terminations. Individual zircons are rounded, with grain widths and lengths ranging from 50 to 110 μm × 90 to 240 μm. The internal morphology of the zircons does not vary significantly in the CL images, with clear oscillatory zones and core-rim structures. The characteristics of the gaps in some zircons indicate that

TABLE 1 Zircon U-Pb results for plagiogranite from Sabei, Huangyangshan, Sujiquan plutons.

Point	Content (×10^{-6})				Isotoperatio						Isotopicage (Ma)					
	^{208}Pb	^{232}Th	^{238}U	Th/U	^{207}Pb/^{206}Pb	σ	^{207}Pb/^{235}U	σ	^{206}Pb/^{238}U	σ	^{207}Pb/^{206}Pb	σ	^{207}Pb/^{235}U	σ	^{206}Pb/^{238}U	σ
SB1-01	2.21	141.03	315.96	0.45	0.053330	0.001430	0.377770	0.013160	0.051270	0.001120	343	41	325	10	322	7
SB1-02	3.49	201.99	340.71	0.59	0.051770	0.001070	0.362990	0.008310	0.050680	0.000730	275	28	314	6	319	4
SB1-03	2.40	147.89	354.18	0.42	0.053800	0.001120	0.366610	0.008200	0.049340	0.000680	363	27	317	6	310	4
SB1-04	2.94	181.88	400.28	0.45	0.053310	0.000940	0.368080	0.006890	0.049930	0.000530	342	24	318	5	314	3
SB1-05	2.49	142.53	365.26	0.39	0.052030	0.002380	0.367590	0.015590	0.051240	0.000890	287	107	318	12	322	5
SB1-06	1.38	79.26	206.64	0.38	0.055220	0.002030	0.386980	0.013550	0.050830	0.000560	421	84	332	10	320	3
SB1-07	2.96	184.96	426.89	0.43	0.053400	0.000870	0.358870	0.005880	0.048740	0.000590	346	18	311	4	307	4
SB1-08	2.67	163.79	394.02	0.42	0.053680	0.000870	0.370280	0.006330	0.049970	0.000600	358	19	320	5	314	4
SB1-09	3.54	223.79	455.42	0.49	0.053500	0.000890	0.361180	0.006370	0.048870	0.000630	350	19	313	5	308	4
SB1-10	1.37	88.13	225.98	0.39	0.054100	0.001640	0.379880	0.012050	0.050900	0.001180	375	34	327	9	320	7
SB1-11	3.74	241.32	495.61	0.49	0.052760	0.001020	0.360930	0.007800	0.049360	0.000910	318	22	313	6	311	6
SB1-12	2.98	178.67	403.69	0.44	0.053400	0.001450	0.364560	0.009650	0.049360	0.000530	346	40	316	7	311	3
SB1-13	2.62	172.38	357.72	0.48	0.053460	0.001300	0.379370	0.010410	0.051090	0.000830	348	34	327	8	321	5
SB1-14	1.30	83.20	177.27	0.47	0.053150	0.001280	0.374040	0.009700	0.050990	0.000740	335	33	323	7	321	5
SB1-15	5.37	318.50	734.71	0.43	0.055300	0.002020	0.386460	0.013080	0.050680	0.000690	424	83	332	10	319	4
SB1-16	3.17	202.84	436.44	0.46	0.052940	0.000820	0.369970	0.006710	0.050540	0.000590	326	21	320	5	318	4
SB1-17	3.07	163.06	421.18	0.39	0.053220	0.003770	0.370910	0.025170	0.050550	0.001020	338	163	320	19	318	6
SB1-18	3.29	199.57	429.15	0.47	0.053230	0.000820	0.377220	0.005680	0.051420	0.000610	338	16	325	4	323	4
SB1-19	2.59	167.79	375.95	0.45	0.051230	0.000900	0.356770	0.007200	0.050460	0.000620	251	25	310	5	317	4
HYS1-01	4.54	267.75	436.23	0.61	0.052120	0.000960	0.356170	0.006490	0.049540	0.000540	291	23	309	5	312	3

(Continued on the following page)

10.3389/feart.2025.1601135

TABLE 1 (*Continued*) Zircon U-Pb results for plagiogranite from Sabei, Huangyangshan, Sujiquan plutons.

Point	Content (×10^{-6})				Isotoperatio						Isotopicage (Ma)					
	^{208}Pb	^{232}Th	^{238}U	Th/U	^{207}Pb/^{206}Pb	σ	^{207}Pb/^{235}U	σ	^{206}Pb/^{238}U	σ	^{207}Pb/^{206}Pb	σ	^{207}Pb/^{235}U	σ	^{206}Pb/^{238}U	σ
HYS1-02	8.60	481.34	620.90	0.78	0.052030	0.002820	0.364150	0.018800	0.050770	0.000820	287	127	315	14	319	5
HYS1-03	2.12	128.83	331.83	0.39	0.052410	0.000840	0.358030	0.005930	0.049500	0.000600	303	18	311	4	311	4
HYS1-04	1.88	99.77	258.50	0.39	0.055970	0.003230	0.393090	0.021780	0.050940	0.000820	451	132	337	16	320	5
HYS1-05	4.94	297.63	590.77	0.50	0.051890	0.000810	0.365670	0.006140	0.050970	0.000610	281	19	316	5	320	4
HYS1-06	1.90	100.78	304.29	0.33	0.054880	0.002540	0.382640	0.016570	0.050570	0.000830	407	106	329	12	318	5
HYS1-07	2.59	153.97	310.42	0.50	0.052350	0.000900	0.368500	0.006280	0.051000	0.000550	301	20	319	5	321	3
HYS1-08	6.04	368.07	531.53	0.69	0.052390	0.001160	0.364670	0.007410	0.050600	0.000690	302	23	316	6	318	4
HYS1-09	4.16	253.68	398.62	0.64	0.052230	0.000880	0.367140	0.005940	0.051010	0.000540	295	19	318	4	321	3
HYS1-10	2.59	159.41	302.49	0.53	0.053160	0.000900	0.367520	0.006600	0.050150	0.000600	336	21	318	5	315	4
HYS1-11	1.36	77.78	179.80	0.43	0.053130	0.001210	0.377880	0.008540	0.051700	0.000770	334	26	325	6	325	5
HYS1-12	0.72	42.59	117.92	0.36	0.053130	0.001520	0.367620	0.010340	0.050490	0.000730	334	38	318	8	318	4
HYS1-13	2.12	130.94	308.80	0.42	0.052950	0.001160	0.360810	0.007390	0.049570	0.000640	327	24	313	6	312	4
HYS1-14	2.26	140.13	274.71	0.51	0.052780	0.000970	0.359320	0.006710	0.049290	0.000500	320	24	312	5	310	3
HYS1-15	12.47	766.04	850.62	0.90	0.052060	0.000570	0.362260	0.005070	0.050290	0.000550	288	15	314	4	316	3
HYS1-16	1.22	78.07	235.61	0.33	0.053480	0.001090	0.365080	0.007590	0.049550	0.000630	349	25	316	6	312	4
HYS1-17	3.45	206.05	370.41	0.56	0.051420	0.000870	0.354760	0.006160	0.049980	0.000520	260	22	308	5	314	3
SJQ1-01	3.14	194.50	440.06	0.44	0.053730	0.001210	0.367200	0.008610	0.049880	0.000960	360	24	318	6	314	6
SJQ1-02	5.47	336.01	881.45	0.38	0.053620	0.000840	0.379880	0.007880	0.051510	0.000810	355	22	327	6	324	5
SJQ1-03	4.84	315.23	760.23	0.41	0.053370	0.000880	0.378660	0.009860	0.051410	0.000880	344	30	326	7	323	5
SJQ1-04	4.27	262.06	561.53	0.47	0.053700	0.001250	0.371230	0.008050	0.050140	0.000760	359	24	321	6	315	5
SJQ1-05	3.23	201.63	496.38	0.41	0.054110	0.001060	0.374700	0.009280	0.050370	0.000880	376	27	323	7	317	5

(Continued on the following page)

10.3389/feart.2025.1601135

TABLE 1 (*Continued*) Zircon U-Pb results for plagiogranite from Sabei, Huangyangshan, Sujiquan plutons.

Point	Content (×10^{-6})				Isotoperatio						Isotopicage (Ma)					
	^{208}Pb	^{232}Th	^{238}U	Th/U	^{207}Pb/^{206}Pb	σ	^{207}Pb/^{235}U	σ	^{206}Pb/^{238}U	σ	^{207}Pb/^{206}Pb	σ	^{207}Pb/^{235}U	σ	^{206}Pb/^{238}U	σ
SJQ1-06	1.21	77.62	174.31	0.45	0.053240	0.001410	0.376060	0.012020	0.051320	0.000940	339	40	324	9	323	6
SJQ1-07	8.44	531.26	1239.19	0.43	0.053930	0.000600	0.376990	0.004800	0.050780	0.000510	368	13	325	4	319	3
SJQ1-08	1.31	82.69	170.20	0.49	0.053520	0.001210	0.370540	0.008650	0.050470	0.000640	351	30	320	6	317	4
SJQ1-09	2.34	144.33	356.43	0.40	0.053110	0.001000	0.378180	0.007760	0.051540	0.000600	334	26	326	6	324	4
SJQ1-10	8.67	554.01	1095.79	0.51	0.052800	0.000850	0.372820	0.007520	0.051260	0.000810	320	21	322	6	322	5
SJQ1-11	4.36	290.66	846.67	0.34	0.052980	0.000740	0.373900	0.005420	0.051120	0.000460	328	17	323	4	321	3
SJQ1-12	2.94	191.66	453.04	0.42	0.052700	0.001060	0.368570	0.008200	0.050680	0.000630	316	29	319	6	319	4
SJQ1-13	4.31	275.08	603.99	0.46	0.053740	0.000930	0.374870	0.007830	0.050400	0.000700	360	24	323	6	317	4
SJQ1-14	2.22	136.02	320.21	0.42	0.052890	0.001050	0.380300	0.009380	0.051750	0.000680	324	33	327	7	325	4
SJQ1-15	2.39	152.18	345.27	0.44	0.053090	0.000970	0.369160	0.006950	0.050370	0.000550	333	24	319	5	317	3
SJQ1-16	0.50	30.80	77.59	0.40	0.053520	0.002010	0.363460	0.012620	0.049640	0.000760	351	51	315	9	312	5
SBMME1-01	5.30	335.55	669.28	0.50	0.053080	0.000740	0.374290	0.007570	0.051190	0.000840	332.0	21	323	6	322	5
SBMME1-02	2.29	135.40	312.47	0.43	0.054510	0.001240	0.363610	0.009330	0.048500	0.000780	392.0	30	315	7	305	5
SBMME1-03	2.22	134.07	310.89	0.43	0.054160	0.000850	0.380450	0.008250	0.051060	0.000880	378.0	22	327	6	321	5
SBMME1-04	4.59	271.00	586.89	0.46	0.054280	0.000790	0.383040	0.007090	0.051370	0.000790	383.0	19	329	5	323	5
SBMME1-05	4.16	223.42	510.96	0.44	0.054940	0.002960	0.390150	0.019770	0.051500	0.000950	410.0	124	334	14	324	6
SBMME1-06	2.35	149.63	341.51	0.44	0.054250	0.001070	0.372810	0.008900	0.049800	0.000740	382.0	28	322	7	313	5
SBMME1-07	4.47	265.49	544.60	0.49	0.054370	0.001080	0.371630	0.007750	0.049660	0.000720	386.0	23	321	6	312	4
SBMME1-08	1.63	102.70	247.05	0.42	0.054310	0.001500	0.368720	0.010110	0.049510	0.000760	384.0	35	319	7	311	5
SBMME1-09	5.56	349.52	656.72	0.53	0.053730	0.000870	0.361480	0.007240	0.048800	0.000690	360.0	22	313	5	307	4
SBMME1-10	2.57	153.23	349.44	0.44	0.054040	0.003540	0.369540	0.023490	0.049600	0.000780	373.0	151	319	17	312	5

(Continued on the following page)

10.3389/feart.2025.1601135

TABLE 1 (*Continued*) Zircon U-Pb results for plagiogranite from Sabei, Huangyangshan, Sujiquan plutons.

Point	Content (x10^{-6})				Isotoperatio						Isotopicage (Ma)					
	^{208}Pb	^{232}Th	^{238}U	Th/U	^{207}Pb/^{206}Pb	σ	^{207}Pb/^{235}U	σ	^{206}Pb/^{238}U	σ	^{207}Pb/^{206}Pb	σ	^{207}Pb/^{235}U	σ	^{206}Pb/^{238}U	σ
SBMME1-11	2.74	171.18	334.60	0.51	0.053220	0.001020	0.368330	0.007930	0.050210	0.000660	338.0	26	318	6	316	4
SBMME1-12	5.90	388.32	663.16	0.59	0.053440	0.001000	0.361310	0.007990	0.049050	0.000670	348.0	27	313	6	309	4
SBMME1-13	1.73	107.69	278.19	0.39	0.052960	0.001120	0.361380	0.008740	0.049440	0.000700	327.0	30	313	7	311	4
SBMME1-14	3.31	210.17	401.74	0.52	0.052370	0.001000	0.372110	0.009890	0.051340	0.000910	302.0	31	321	7	323	6

they may have been affected by dissolution at some point. Th and U contents of 102.70–388.32 ppm and 247.05–669.28 ppm are obtained, respectively, with Th/U ratios of 0.39–0.59. The morphology, structure, and Th/U ratio of the zircons indicate a magmatic origin for this group of zircons. The weighted average $^{206}Pb/^{238}U$ age of 313.9 ± 3.5 Ma (MSWD = 1.7, n = 14) (Figure 3d) likely represents the crystallization age of the MMEs, i.e., the Late Carboniferous, which is similar to that of the host monzogranite.

5.2 Whole-rock major elements

The results for the whole-rock major, trace, and rare earth elements (REEs) in the Sabei, Huangyangshan, and Sujiquan plutons and the MMEs are listed in Table 2. The three plutons have high contents of silicon (76.30–77.41 wt%), potassium (4.04–4.67 wt%), alkali ($Na_2O + K_2O$ = 8.18–8.80 wt%), and Na_2O (3.98–4.40 wt%); the total alkali mass fraction exceeds 8%, indicating the rock is subalkaline. The Mg# value ranges from 8.6 to 35.3. The aluminum saturation index (A/CNK) is 0.94–0.99, and A/NK is 0.97–1.06.

The MMEs have lower contents of SiO_2 (55.37–67.33 wt%) and total alkali ($Na_2O + K_2O$) (5.89–7.00 wt%) than the host rock, indicating a diorite composition. The TFeO (3.47–7.57 wt%), MgO (1.27–5.26 wt%), and CaO (3.05–6.97 wt%) contents are significantly higher than those of the host granite, and the Al_2O_3 content is higher (14.93–16.26 wt%), indicating aluminum supersaturation (A/CNK = 1.26–1.49). However, the enclaves are relatively enriched in P_2O_5 (0.13–0.17 wt%) and Mg# (44.2–55.3). The values are slightly higher than those of the host rocks, suggesting a mantle melt composition.

All host rock samples from Sabei, Huangyangshan, and Sujiquan fall into the granite field of the total alkali-silica (TAS) diagram (Figure 4a), with MMEs falling into the granodiorite and monzodiorite areas. The host rock samples show weak peralkaline-metaluminous characteristics in the A/CNK-A/NK diagram (Figure 4b), whereas the MME samples are peraluminous. Most of the host rock samples and MMEs fall into the high-K calc-alkaline series of the SiO_2-K_2O diagram (Figure 4c).

The Harker diagram (Figures 5a–h) indicates that the host granite samples plot in a concentrated zone, indicating a linear relationship between host granites and MMEs. Al_2O_3, MgO, CaO, MnO, FeO, TiO_2, and TFe_2O_3 are negatively correlated with SiO_2; K_2O is positively correlated with SiO_2; TFeO is positively correlated with MgO; and Na_2O shows no linear relationship with SiO_2. Excellent linear correlations are observed for the dominant oxide ratios: Na_2O/CaO vs. Al_2O_3/CaO, Na_2O/CaO vs. SiO_2/CaO, SiO_2/MgO vs. Al_2O_3/MgO, and CaO/MnO vs. MgO/MnO (Figure 6).

5.3 Trace and rare earth element

The results of the rare earth and trace element analyses for the Sabei, Huangyangshan, and Sujiquan plutons and the Sabei MMEs in the eastern KGB are listed in Table 2. The granite samples from the Sabei, Huangyangshan, and Sujiquan host rocks in the Karamaili East section exhibit elevated ΣREE contents ranging from 121.78 to 261.32 ppm, with Σ light REEs (LREEs) ranging from 81.23 to

TABLE 2 Major (%), trace ($\times10^{-6}$), and rare earth elemental ($\times10^{-6}$) compositions of rocks from the Sabei, Huangyangshan, and Sujiquan plutons.

Pluton	Sabei Pluton				Huangyangshan Pluton				Sujiquan Pluton				MMEs		
Sample	SB1	SB2	SB3	SB4	HYS1	HYS2	HYS3	HYS4	SJQ1	SJQ2	SJQ3	SJQ4	SBMME1	SBMME2	SBMME3
SiO_2	76.30	76.92	77.41	77.29	76.61	76.37	77.49	76.61	77.30	76.72	77.12	77.38	67.33	55.37	63.29
TiO_2	0.05	0.22	0.07	0.07	0.04	0.06	0.09	0.08	0.10	0.08	0.07	0.07	0.52	0.88	0.70
Al_2O_3	12.14	11.25	11.51	12.15	12.29	12.28	11.54	12.29	11.50	12.11	12.17	11.97	14.93	16.26	15.59
TFe_2O_3	1.41	1.84	1.18	0.71	0.98	0.89	0.97	1.09	1.72	0.95	0.75	0.88	3.47	7.57	5.52
FeO	0.46	0.69	0.78	0.44	0.46	0.81	0.75	0.31	0.84	0.57	0.50	0.38	1.61	4.73	3.17
MnO	0.03	0.05	0.01	0.03	0.04	0.01	0.02	0.02	0.04	0.02	0.04	0.02	0.08	0.19	0.13
MgO	0.09	0.16	0.10	0.19	0.06	0.07	0.26	0.25	0.09	0.21	0.23	0.18	1.71	5.26	2.45
CaO	0.40	0.21	0.35	0.21	0.42	0.41	0.45	0.46	0.19	0.36	0.42	0.39	3.05	6.97	4.37
Na_2O	4.14	3.98	4.28	4.21	4.23	4.38	4.08	3.99	4.28	4.40	4.24	4.25	3.49	4.19	3.38
K_2O	4.51	4.67	4.04	4.59	4.30	4.38	4.10	4.62	4.26	4.34	4.25	4.31	3.51	1.70	2.89
P_2O_5	0.01	0.03	0.01	0.02	0.01	0.01	0.02	0.03	0.02	0.01	0.02	0.01	0.13	0.17	0.15
LOI	0.57	0.39	0.56	0.23	0.35	0.83	0.79	0.28	0.26	0.57	0.51	0.38	1.10	1.24	1.17
Total	99.65	99.74	99.52	99.70	99.31	99.69	99.81	99.72	99.77	99.77	99.82	99.84	99.33	99.81	99.66
Tzr (°C)	839	798	733	789	797	796	803	838	892	788	815	789	739	654	718
A/CNK	0.98	0.94	0.95	0.99	0.99	0.97	0.96	0.99	0.96	0.96	0.99	0.97	0.99	0.76	0.94
A/NK	1.04	0.97	1.01	1.02	1.06	1.03	1.03	1.06	0.99	1.01	1.05	1.03	1.56	1.86	1.79
$Na_2O + K_2O$	8.65	8.66	8.32	8.80	8.53	8.76	8.18	8.61	8.54	8.74	8.49	8.56	7.00	5.89	6.27
K_2O/Na_2O	1.09	1.17	0.94	1.09	1.02	1.00	1.00	1.16	1.00	0.99	1.00	1.01	1.01	0.41	0.86
AR	5.44	7.17	5.70	5.94	5.09	5.46	5.29	5.16	6.43	5.69	5.14	5.51	2.28	1.68	1.92
Sc	1.1	1.8	3.5	4.2	1.5	1.8	1.5	3.4	1.1	2.6	3.2	2.6	8.5	18.2	15.4
V	2.3	3.6	16.0	25.8	2.2	10.9	18.2	2.0	2.6	11.2	1.8	3.9	37.6	125.4	94.5

(Continued on the following page)

10.3389/feart.2025.1601135

TABLE 2 (*Continued*) Major (%), trace ($\times10^{-6}$), and rare earth elemental ($\times10^{-6}$) compositions of rocks from the Sabei, Huangyangshan, and Sujiquan plutons.

Pluton	Sabei Pluton				Huangyangshan Pluton				Sujiquan Pluton				MMEs		
Sample	SB1	SB2	SB3	SB4	HYS1	HYS2	HYS3	HYS4	SJQ1	SJQ2	SJQ3	SJQ4	SBMME1	SBMME2	SBMME3
Cr	2.3	4.2	7.6	8.7	1.8	5.2	68.9	0.9	2.5	5.6	1.0	0.9	12.5	128.6	40.6
Co	2.0	2.2	3.5	1.1	2.0	2.0	0.5	0.4	2.0	2.6	0.4	0.3	11.2	22.4	18.8
Ni	1.2	1.8	4.3	5.3	0.5	2.7	5.1	0.8	1.5	3.0	0.8	0.5	9.9	50.0	29.9
Cu	4.7	7.6	13.3	3.8	25.9	11.3	2.4	3.8	5.5	11.6	4.1	2.4	17.2	75.2	56.2
Zn	133.9	135.2	121.5	52.3	106.3	128.3	50.9	48.7	111.3	114.7	49.1	42.9	48.4	92.3	77.3
W	0.5	0.5	0.7	0.6	1.5	0.8	0.6	0.8	0.2	0.7	0.5	0.8	0.5	2.5	1.6
Ga	28.6	20.7	18.9	25.3	22.8	19.9	25.9	26.2	22.7	20.5	25.7	23.9	14.8	17.4	16.8
Rb	228.8	210.6	178.5	345.9	333.6	194.5	358.1	332.4	146.2	231.1	335.3	321.8	112.3	69.3	98.8
Sr	6.1	7.8	6.5	3.9	3.2	5.3	5.8	11.6	3.8	37.5	11.7	7.3	298.3	297.3	290.4
Y	153.2	48.9	141.5	115.8	122.3	114.6	156.2	98.9	54.1	103.8	99.8	95.6	23.0	48.2	38.6
Zr	292.6	194.5	87.2	165.7	181.2	187.3	197.2	285.6	503.2	169.8	221.9	169.5	107.9	79.8	98.9
Nb	15.2	17.2	7.8	17.9	16.5	9.2	15.8	15.9	10.3	12.7	14.9	12.8	5.3	8.3	7.2
Ba	8.0	8.2	9.7	27.0	6.1	19.3	7.2	31.9	17.4	54.2	30.7	7.9	379.9	162.3	275.1
Hf	10.6	10.0	4.2	9.1	8.8	9.0	10.8	13.9	10.7	7.8	10.8	9.1	3.4	2.9	3.3
Ta	1.3	1.1	0.9	2.9	1.7	1.2	1.5	2.4	0.8	1.5	2.8	1.9	0.7	0.8	0.8
Pb	33.4	30.7	41.3	29.7	28.4	37.3	41.2	29.8	7.5	35.1	30.9	29.8	11.9	7.1	10.0
Th	19.5	17.7	12.9	35.5	17.7	15.6	41.7	28.7	7.3	18.7	33.8	32.9	11.2	5.4	8.9
U	8.0	4.5	6.5	5.9	3.9	4.2	6.8	3.9	2.0	4.9	3.1	3.8	2.2	4.3	3.4
La	38.63	35.27	15.24	31.90	15.98	19.57	12.57	28.90	41.25	24.10	30.74	19.15	16.38	20.09	19.23
Ce	102.01	98.61	35.57	73.60	36.95	29.16	35.70	65.12	96.89	56.73	70.81	48.94	29.66	48.69	35.18
Pr	11.36	4.27	3.13	10.39	6.34	4.20	5.17	9.71	12.13	6.14	9.94	8.67	4.64	8.33	6.68

(Continued on the following page)

10.3389/feart.2025.1601135

TABLE 2 (*Continued*) Major (%), trace (×10^{-6}), and rare earth elemental (×10^{-6}) compositions of rocks from the Sabei, Huangyangshan, and Sujiquan plutons.

Pluton	Sabei Pluton				Huangyangshan Pluton				Sujiquan Pluton				MMEs		
Sample	SB1	SB2	SB3	SB4	HYS1	HYS2	HYS3	HYS4	SJQ1	SJQ2	SJQ3	SJQ4	SBMME1	SBMME2	SBMME3
Nd	39.92	37.44	18.96	42.90	24.19	19.27	21.74	31.80	45.98	27.59	36.90	31.84	15.91	30.57	25.24
Sm	10.21	3.48	9.75	12.61	7.68	8.91	8.11	9.87	10.26	7.94	10.15	11.81	3.76	7.09	5.78
Eu	0.02	0.09	0.34	0.05	0.01	0.12	0.04	0.03	0.08	0.16	0.05	0.03	0.80	0.97	0.91
Gd	11.01	10.21	4.25	10.51	8.13	8.23	7.89	9.51	9.68	7.96	9.67	9.15	3.81	6.69	5.52
Tb	1.82	1.89	0.94	2.39	1.49	1.73	2.15	2.34	1.31	1.54	2.84	1.97	0.52	0.96	0.85
Dy	16.33	14.26	7.24	16.80	12.42	10.61	13.47	15.11	8.82	11.65	14.61	15.39	3.57	6.87	5.22
Ho	3.06	3.84	3.42	3.51	2.43	2.97	4.15	3.01	1.64	2.21	2.98	3.41	0.70	1.30	1.00
Er	11.43	9.17	10.61	9.98	8.21	7.29	12.91	9.24	5.24	8.50	9.02	9.39	2.36	4.53	3.74
Tm	1.74	1.58	1.20	2.07	1.28	1.31	2.91	2.37	0.78	1.38	2.35	2.41	0.36	0.74	0.65
Yb	11.96	9.71	13.51	13.07	8.94	9.21	18.61	13.07	4.67	10.01	12.83	12.89	2.55	5.01	3.88
Lu	1.83	1.74	0.94	1.97	1.31	1.29	2.81	1.72	0.80	1.38	1.29	1.71	0.40	0.86	0.66
ΣREE	261.33	231.56	122.65	231.75	135.36	121.78	148.23	201.80	239.54	167.28	214.18	176.76	85.42	142.70	114.54
LREE	202.15	179.16	82.99	171.45	91.15	81.23	83.33	145.43	206.60	122.65	158.59	120.44	71.15	115.74	93.02
HREE	59.18	52.40	39.66	60.30	44.21	40.55	64.90	56.37	32.94	44.63	55.59	56.32	14.27	26.96	21.52
LREE/HREE	3.42	3.42	2.09	2.84	2.06	2.00	1.28	2.58	6.27	2.75	2.85	2.14	4.99	4.29	4.32
(La/Sm)N	2.38	6.38	0.98	1.59	1.31	1.38	0.98	1.84	2.53	1.91	1.91	1.02	2.74	1.78	2.09
(La/Yb)N	2.18	2.45	0.76	1.65	1.21	1.43	0.46	1.49	5.96	1.62	1.62	1.00	4.33	2.70	3.34
Mg#	10.5	13.5	13.1	32.3	9.8	12.3	32.3	29.0	8.6	28.3	35.3	26.7	46.8	55.3	44.2

Note: A/CNK, molar (Al_2O_3/(Cao + K_2O + Na_2O)); Mg #, 100× MgO/(MgO+0.505× (Fe_2O_3 × 0.9+FeO)), assuming that FeO is equal to 90% of the total Fe oxide; δEu, $Eu_N \times 2/(Sm_N + Gd_N)$, and the subscript "N" indicates chondrite standardization (Sun and Mc Donough, 1989).

10.3389/feart.2025.1601135

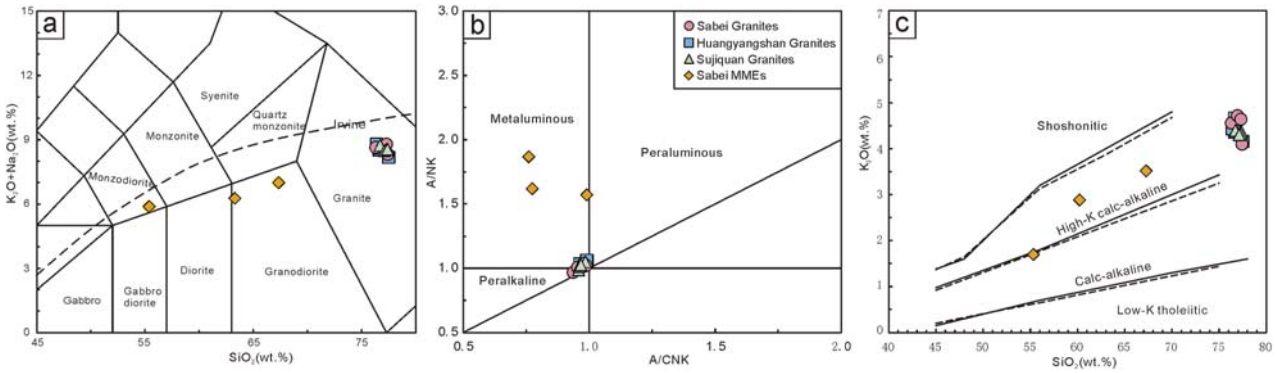

FIGURE 4
Classification of MMEs and their host granitoids. **(a)** ($K_2O + Na_2O$) vs. SiO_2 (after Middlemost (1994)), **(b)** A/NK vs. A/CNK (after Maniar and Piccoli (1989)), and **(c)** SiO_2 vs. AR (after Wright (1969)).

206.60 ppm and Σ heavy REEs (HREEs) from 32.94 to 64.90 ppm. The ΣLREE/ΣHREE ratio is 1.28–6.27.

The chondrite-normalized REE patterns for the granite samples from the Karamaili belt display a deep V-shaped distribution and a negative Eu anomaly ($Eu/Eu^* = 0.01–0.34$) (Figure 7a). The host granites and MMEs exhibit the same signatures in the primitive mantle-normalized trace element spider diagram (Figure 7b), characterized by systematic incompatible element enrichment, particularly in high field strength elements (HFSEs). Negative anomalies are observed at Ba, Sr, P, and Ti, while positive anomalies occur at Rb, Th, K, and the Zr-Hf pair. All samples display systematic Nb-Ta depletion relative to adjacent elements (Th, K, La-Ce). A spider diagram of the trace elements normalized to the primitive mantle indicates substantial Ba, Sr, P, Eu, and Ti depletion and relative depletion in Tb and Tm. HFSEs (Ta, Th, U) and LILEs (Rb, K, Pb) are relatively enriched (Figure 7b). The granite zircon chondrite-normalized REE patterns reveal considerable LREE depletion and HREE enrichment, with La to Lu values showing a variation over five to six orders of magnitude, and a strong negative Eu anomaly (Figure 7c). In contrast, no LREE and HREE fractionation is observed in the zircons from the MME, with only a slight negative Eu anomaly (Figure 7d), indicative of plagioclase fractionation or retention during magma evolution, as Eu replaces Ca in plagioclase.

5.4 Whole rock Nd isotopes

Four samples were collected from the KGB for whole-rock Nd isotope analysis (Table 3), with four samples from the Sabei pluton (SB-1, SB-3, SBMME-1, SBMME-2), one from the Huangyangshan pluton (HYS-1), and one from the Sujiquan pluton (SJ-1).

Table 3 shows that the Sm/Nd ratios for the Sabei, Huangyangshan, and Sujiquan plutons range from 0.135 to 0.156, with similar ratios for different rock types, implying a uniform source material and a relatively closed Sm-Nd system during petrogenesis. These values are lower than the chondritic $^{147}Sm/^{144}Nd$ ratio of 0.1967 (Hamilton et al., 1983). The $^{143}Nd/^{144}Nd$ ratios of 0.512787–0.512808 and εNd(t) values for the Sabei, Huangyangshan, and Sujiquan rocks fall in the range +4.0 to +4.5, with T_{2DM} values ranging from 608 to 651.

In contrast, the SBMMEs exhibit higher Sm/Nd ratios (0.196–0.230), $^{143}Nd/^{144}Nd$ ratios from 0.512921 to 0.512965, and εNd(t) values from +5.5 to +5.7. T_{2DM} values of 476–488 are obtained for the Sabei MMEs.

6 Discussions

6.1 Time constraints for plutons

The Carboniferous was the critical stage of tectonic transformation in Eastern Junggar. Therefore, constraining the evolutionary period of siliceous magmatic activity in the Karamaili area is crucial (Chen et al., 2010; Zhang et al., 2010; Li et al., 2015). Previous studies have suggested that the emplacement time in the KGB was 328–283 Ma (Han et al., 2006; Lin et al., 2007; Su et al., 2008; Tang et al., 2009; Yang et al., 2009; Gan et al., 2010; Han et al., 2012). In this study, the LA-ICP-MS zircon U-Pb ages for the Sabei monzogranite, Huangyangshan biotite syenogranite, and Sujiquan biotite granite are 315.9 ± 2.4 Ma, 316.1 ± 2.2 Ma, and 319.4 ± 2.0 Ma, respectively. These ages indicate that the emplacement time of the plutons in the eastern section of the KGB can be constrained to 320–315 Ma. The LA-ICP-MS zircon U-Pb age for the MMEs of the Sabei pluton is 313.9 ± 3.5 Ma. Field investigations reveal no discernible intrusive contacts between host granites and MMEs. Consequently, the geochronological data indicate that both lithological units have similar emplacement ages within the analytical uncertainty. It has been suggested that MMEs and granitic plutons are products of the synchronous evolution of the magma.

6.2 Petrogenesis of the granites and MMEs

The granites in the Sabei, Huangyangshan and Sujiquan plutons are characterized by high Si, K, and alkali contents. The CaO, MgO, Ta, Ba and TiO_2 contents are low, with $10,000 \times Ga/Al = 3.06–4.45$. These values are significantly higher than the average

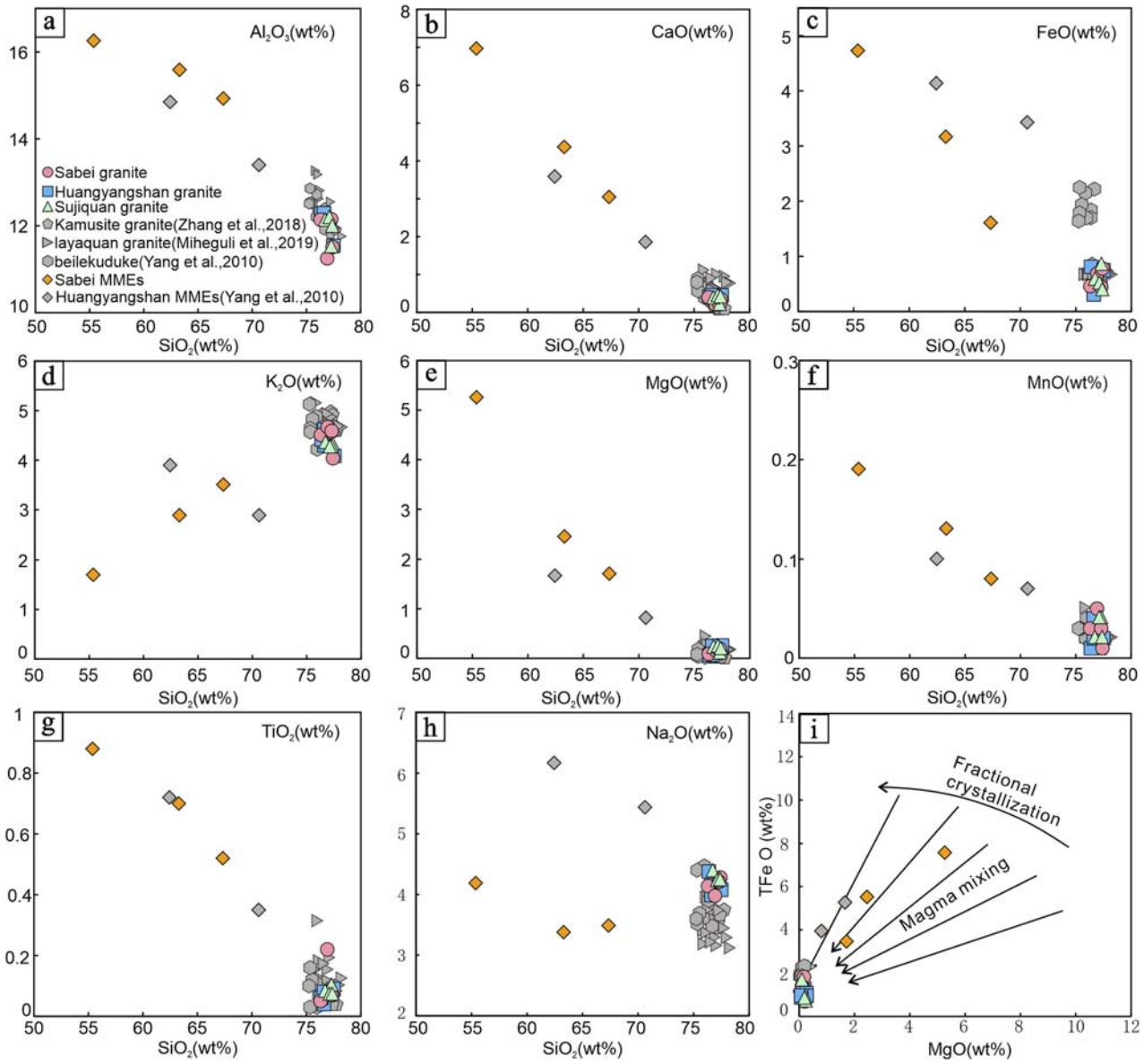

FIGURE 5
(a–h) SiO_2 vs. major oxide variation diagrams of MMEs and host granites. **(i)** MgO vs. TFeO (after Zorpi et al. (1991)).

values for I-type and S-type granites (2.10 and 2.28) and the relatively enriched HFSEs (Ta, Th, U) and LILEs (Rb, K, Pb), indicating geochemical characteristics similar to those of A-type granite. The strong negative Eu anomalies (δEu = 0.01–0.34) and low Sr contents (3.2–37.5 ppm, mean = 9.2 ppm) differentiate these granites from highly fractionated I-type granite, They are important indicators of A-type granite (Xu et al., 2015). The whole-rock zircon saturation temperatures of the granites range from 735 °C to 895 °C, with most samples showing higher temperatures than typical zircon saturation temperatures of highly-fractionated I-type granite (average 764 °C) (Alberto and Patino, 1997; King et al., 1997). This finding indicates that the magma partially melted under water-deficient conditions at temperatures of >830 °C, which is a typical A-type granite formation condition.

The KGB samples fall in the A-type granite area of the TFeO/MgO vs. 10000 Ga/Al discrimination diagram (Figure 8a), indicating they differ from the I- and S-types. The geochemical characteristics are similar for A-type and highly fractionated I-type granites (King et al., 1997). Most of the Sabei, Huangyangshan, and Sujiquan pluton samples fall within the A-type granite area in the $(K_2O + Na_2O)/CaO$ vs. Zr + Nb + Ce + Y diagram (Figure 8b). Thus, they differ from the samples derived from the Kamusite and Laoyaquan plutons in the western part of the KGB, which fall within the highly differentiated I-type granite. The samples from the KGB fall within the A2-type granite area in the Nb, Y, Ce, and Yb classification diagrams (Figures 8c,d), indicating orogenic A-type granite genesis. It differs from the non-orogenic A_1-type granite, and the magma source has an affinity with island-arc basalts

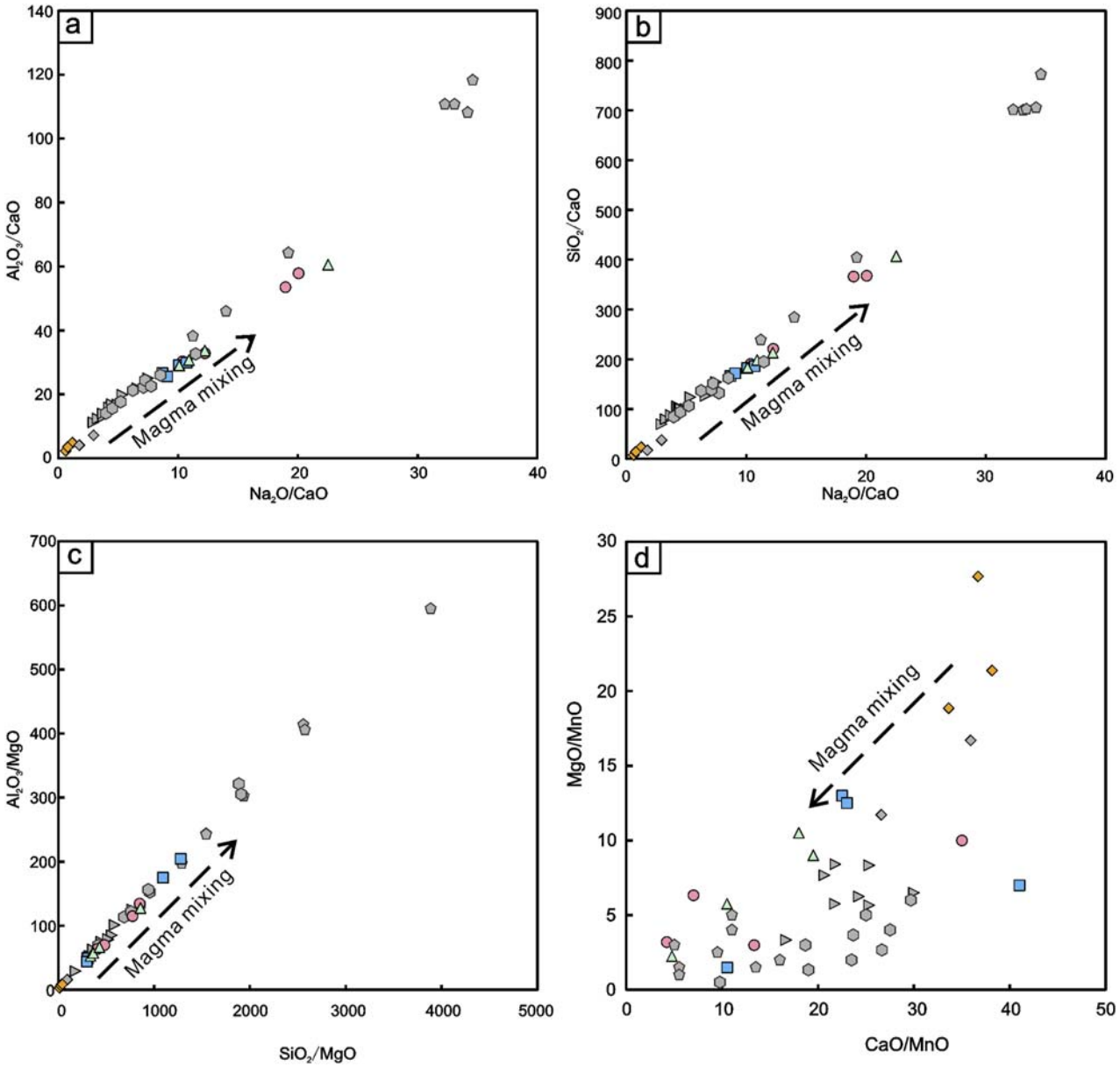

FIGURE 6
Diagram showing predominant oxide ratios of MMEs and host granites. **(a)** Al_2O_3/CaO vs. Na_2O/CaO diagrams of MMEs and host granites; **(b)** SiO_2/CaO vs. Na_2O/CaO diagrams of MMEs and host granites; **(c)** Al_2O_3/CaO vs. SiO_2/MgO diagrams of MMEs and host granites; **(d)** MgO/MnO vs. CaO/MnO diagrams of MMEs and host granites (Symbols/key consistent with Figure 5).

(IABs). These results, in conjunction with the geological features, including the location of the KGB at the plate margin and the delayed timing of ocean basin closure and subduction, suggest that the Sabei, Huangyangshan, and Sujiquan granites are typical quasi-aluminous, alkaline-high-potassium calc-alkaline A_2-type granites.

MMEs with different numbers, sizes, and shapes are widely observed in the Sabei and Huangyangshan plutons. The genesis of these enclaves is generally determined using four approaches: refractory residues of granite protolith melting (Chappell et al., 1987; Chappell and White, 1991; White et al., 1999; Chappell and Wyborn, 2012), xenoliths from the wall rock (Maas et al., 1997), the early crystallized cumulates from cognate magma (Noyes et al., 1983; Dahlquist, 2002; Donaire et al., 2005), and the mixing/mingling of magma (Baxter and Feely, 2002; Barbarin, 2005; Słaby and Martin, 2008).

The contacts between MMEs and host granites typically exhibit sharp macroscopic boundaries, occasionally displaying diffuse transitions, with ubiquitous dark fine-grained chilled margins. These textural features preclude an origin as xenoliths from the wall-rock or refractory residues of granite protolith melting. The pluton contains abundant dioritic MMEs characterized by magmatic fine-grained hypidiomorphic granular textures and massive structures, indicative of rapid crystallization under disequilibrium conditions. Petrogenetic constraints suggest that

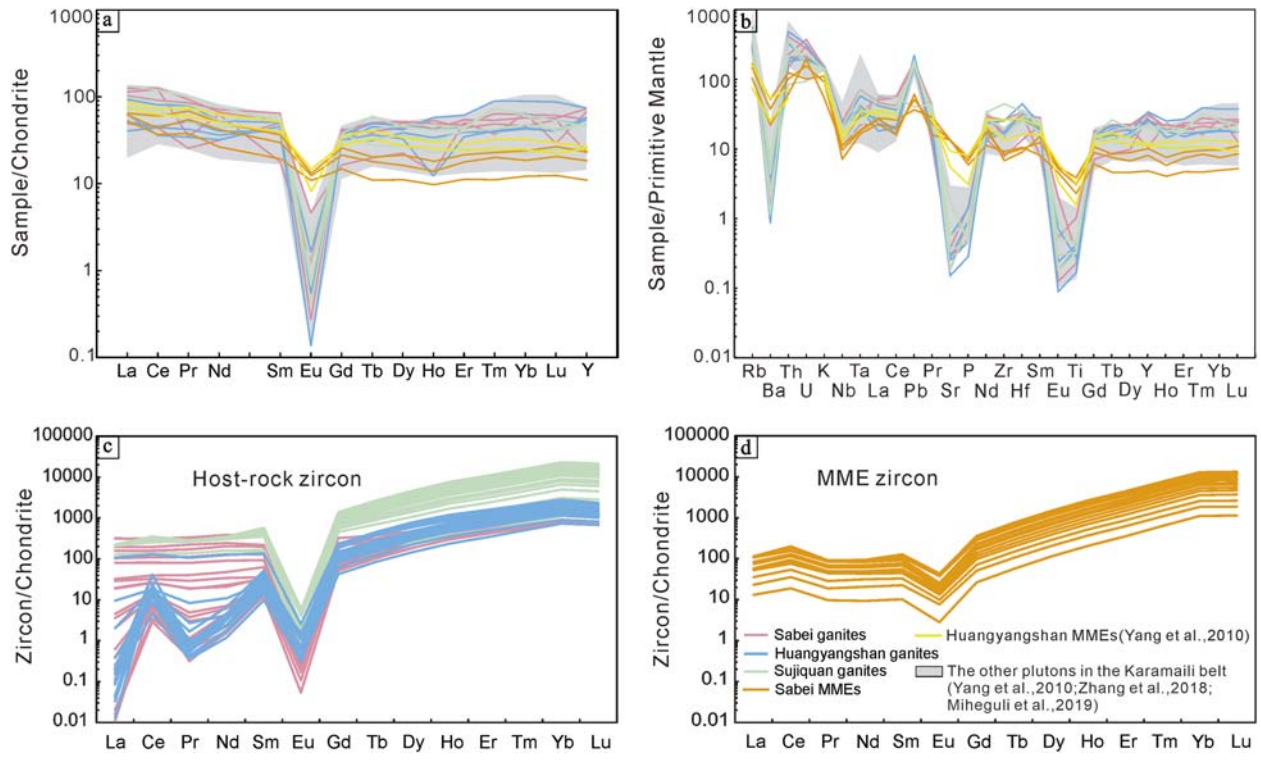

FIGURE 7
Chondrite-normalized REE patterns and primitive mantle-normalized trace element spider-diagrams for **(a,b)** Karamaili host and MMEs sample; and **(c,d)** Karamaili host and MMEs Zircon. Chondrite REE and primitive mantle values were normalized after Sun and Mc Donough (1989).

supercooled mafic magmatic blobs intruded into cooler felsic host magma during magma mixing. This process induced metasomatic replacement of early-crystallized plagioclase, forming K-feldspar reaction rims. The ubiquitous acicular to columnar apatite inclusions in the plagioclase, displaying distinct crystallographic orientations from host rock apatite, represent quench-crystallized products (Barbarin, 1988; Barbarin and Didier, 1992). These textural indicators, particularly the diagnostic acicular apatite morphologies, suggest significant thermal contrast (>200 °C) between mafic enclave-forming magma and host felsic magma, with rapid heat dissipation during crystallization. However, the MMEs are randomly distributed in the host granitoids, and petrological analysis reveals that they have magmatic textures and numerous disequilibrium textures, which are contradictory to autoliths, suggesting they likely formed through magma mixing. Transitional zones at the interfaces reveal plagioclase phenocrysts containing euhedral oscillatory-zoned cores overgrown by multiple generations of anhedral rims, recording episodic growth under fluctuating physicochemical conditions. Sector-zoned textures in the plagioclase indicate dynamic crystallization environments. The presence of relatively coarse-grained amphibole clusters within the MMEs indicates precursory crystallization of mafic phases prior to magma interaction (Zorpi et al., 1991), whereas felsic mineral assemblages formed during later-stage co-crystallization of residual enclave magma and host granodioritic melt under comparable cooling rates (Vernon, 1984). Chemical hybridization through interdiffusion between mafic and granodioritic magma to achieve a local equilibrium resulted in mutual geochemical modification. This petrogenetic mechanism accounts for the observed geochemical similarity in the major/trace element compositions and mineral assemblage between host rocks and MMEs.

In the Harker diagrams of major oxides versus SiO_2 (Figure 5), the samples from this pluton exhibit well-defined negative linear correlations between Al_2O_3, CaO, FeO, K_2O, MgO, MnO, TiO_2, Na_2O, and TFeO with increasing SiO_2 content. These systematic trends strongly suggest magma mixing between host granites and MMEs. Fractional crystallization typically generates trends due to sequential mineral phase removal (e.g., plagioclase and amphibole), whereas mixing systems preserve linear arrays reflecting binary endmember blending. The TFeO-MgO correlation diagram (Figure 5i) supports this interpretation. All compositional data plot along established magma mixing trend lines, indicative of chemical hybridization between mafic and felsic melts. Figure 6 shows well-defined inverse linear correlations in key oxide ratios between MMEs and host granites. These trends reflect potential magma mixing evolutionary trends between the host granite and its enclaves. The primitive mantle-normalized spider diagrams (Figure 7b) reveal broadly parallel patterns between enclaves and host rocks, consistent with assimilation-fractional crystallization (AFC) during coeval magma evolution (Lei et al., 2019). The AFC accounts for the observed geochemical similarity between the dioritic enclaves and granitic hosts, particularly the depletion in Nb, Ta, P, and Ti. These anomalies primarily reflect fractionation of accessory phases (e.g., apatite and Ti-bearing oxides), coupled with

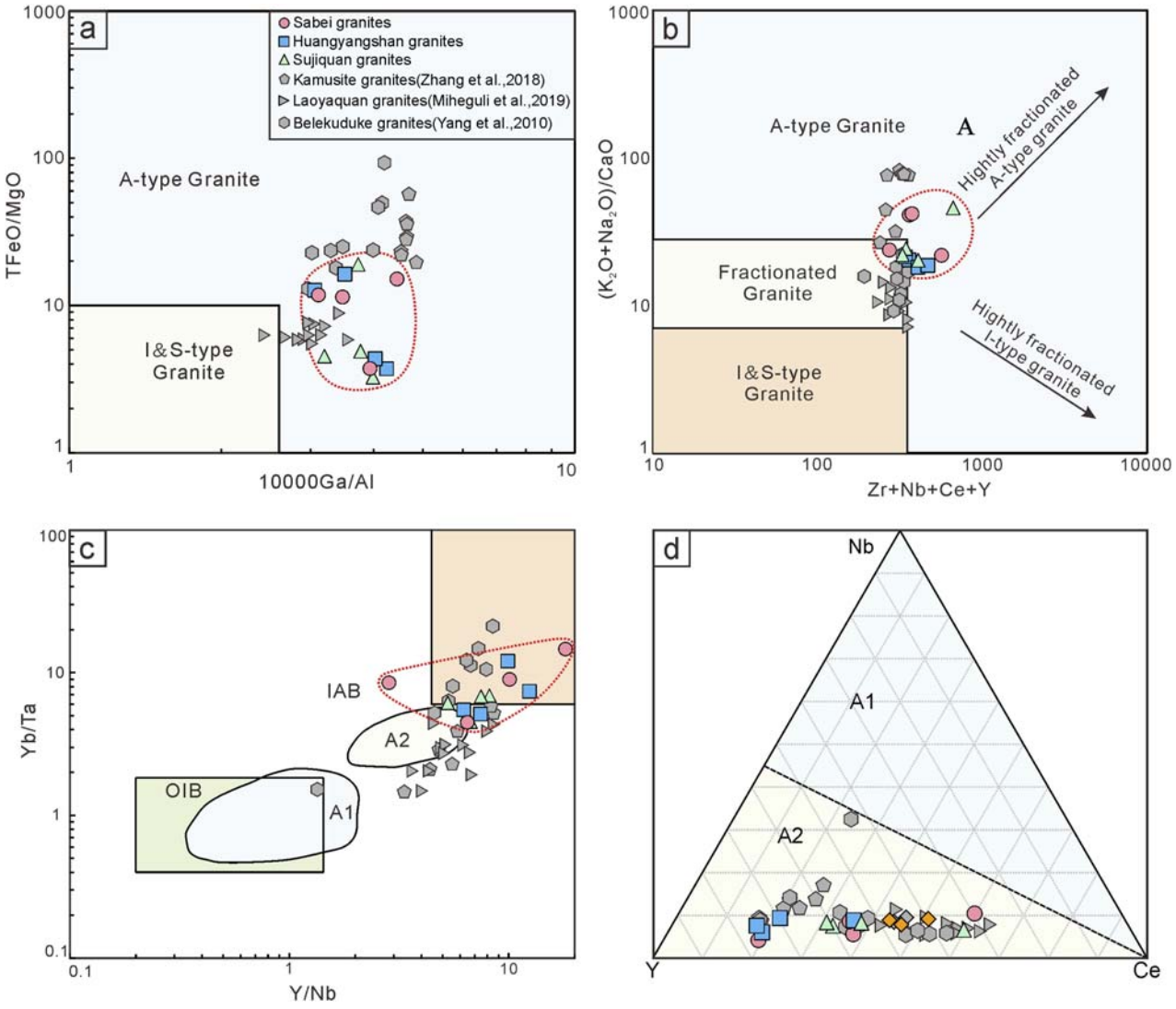

FIGURE 8
Petrogenetic discriminant diagrams. **(a)** TFeO/MgO vs. 10000Ga/Al (from Whalen et al., 1987); **(b)** (K_2O + Na_2O)/CaO vs. Zr + Nb + Ce + Y (from Whalen et al., 1987); **(c)** Yb/Ta vs. Y/Nb; and **(d)** Nb-Y-Ce (from Eby, 1992) (A1 = Intraplate rift or mantle plume; A2 = Post-collisional or post-orogenic).

crustal contamination. The chondrite-normalized REE patterns display analogous LREE-enriched profiles, yet exhibit HREE crossover features between host rocks and enclaves (Figure 7a). This finding suggests that the host granites and enclaves represent distinct but interacting magma batches.

The MMEs of the Sabei plutons exhibit the following features. (1) The zircon geochronology of the MMEs is 313.9 ± 3.5 Ma, whereas the age of the host granite is 315.9 ± 2.4 Ma, showing consistency in the formation chronology. This equivalence precludes the possibilities of refractory residues of granite protolith melting or xenoliths from the wall rock because both source materials would predate the host magma chronology (Brown and Fyfe, 1970; Kempton et al., 1987); (2) The host granite and MMEs exhibit different lithologies. Distinct boundaries exist between the round, oval, or droplet-shaped enclaves and the host rock, and plagioclase with a sieve structure is common (Figure 2e). Therefore, these observations preclude the potential origins of the detachment of the early-stage crystallized homologous magma (O'Hara, 1977). (3) Acicular apatite generally originates from rapidly cooling magma (Wyllie et al., 1962), i.e., its presence indicates rapid cooling. (4) The petrography of the MMEs indicates they have a magmatic origin and do not originate from the surrounding rock; i.e., they are not xenoliths. The similarity in the zircon U-Pb ages indicates that the MMEs and host rocks coexisted and were products of contemporaneous mafic and acidic magmas. (5) The TFeO vs. MgO diagram shows that the MMEs did not evolve along the crystallographic differentiation trend of mafic magma, but were distributed near the magma mixing trend line. This finding indicates an evolution toward the host granite composition (Figure 5i), suggesting that the MMEs are represent hybridized melt blobs left over from the siliceous magma due to magma mixing during the uplift of the mafic magma. The age of the Sabei MMEs is consistent with that of the host granite and the characteristics of the trace elements

10.3389/feart.2025.1601135

TABLE 3 Whole-rock Nd isotope test data for samples from the Eastern Karamaili Belt.

Pluton	Sample	Sm	Nd	$^{147}Sm/^{144}Nd$	$^{143}Nd/^{144}Nd$	2σ	εNd (0)	εNd(t)	2σ	T_{DM}	T_{2DM}	T_{DMC}
Sabei	SB-1	3.11	13.48	0.139577	0.512787	0.000008	+2.9	+4.0	0.08	750	608	615
	SB-3	10.25	39.83	0.155523	0.512805	0.000007	+3.3	+4.1	0.07	908	646	611
	SBMME-1	14.46	44.63	0.195819	0.512921	0.000008	+5.5	+5.5	0.08	1965	488	489
	SBMME-3	6.32	16.58	0.230358	0.512965	0.000008	+6.4	+5.7	0.08	1707	476	473
Huangyangshan	HYS-1	8.94	39.91	0.135395	0.512808	0.000008	+3.3	+4.5	0.08	669	651	575
Sujiquan	SJQ-2	6.92	29.85	0.140099	0.512800	0.000006	+3.2	+4.3	0.06	728	615	595

and REE are similar, indicating a dioritic magmatic enclave. The magma is derived from mantle material and is a product of magma mixing.

6.3 Implications for tectonic setting

The Karamaili ophiolite mélange is considered a fragment of the eastern Karamaili Ocean in the Junggar Ocean (Xu et al., 2015). The expansion of the ocean basin likely occurred from the late Silurian to the late Devonian (Jian et al., 2003; Shu and Wang, 2003; Xu et al., 2011). Subsequently, the Junggar Ocean was subducted under the Siberian Plate at the edge of the continental block, generating accretionary wedges and continental margin volcanic arcs, such as the abundant late Devonian-Early Carboniferous island arcs and volcanic rocks observed in the area (Li, 1995; Zhang and Guo, 2010; Cai et al., 2012).

The Eastern Junggar exhibits the characteristics of a multi-island arc structure, with many island arc belts and fore-arc, and back-arc basins that formed during compression in the Early Carboniferous. Subsequently, the ocean basin closed, the island arcs merged, and the land mass was uplifted by extrusion in the middle Early Carboniferous. During the syn-collision orogenic phase, the subduction orogeny weakened, leading to the slab break-off of the subducted oceanic plate in the late Carboniferous. Subsequently, compression-extension tectonic transformation occurred, gradually transitioning into the post-collision extension stage and causing the underplating of large-scale mantle-derived materials. The basic magma intruded upward and partially melted the upper crustal material, resulting in the formation of large-scale siliceous magma, juvenile crustal growth, and the Late Carboniferous KGB (Han et al., 2006; Su et al., 2006; Gan et al., 2010; Li et al., 2015; Zhang et al., 2020).

As shown in the Y + Nb-Rb diagram, most of the KGB samples fall in the intraplate granite area, indicating a formation environment comprising ridge granite, volcanic arc granite, and syn-collision granite (Figure 9a). The R_1-R_2 and Al_2O_3-SiO_2 diagrams of the post-orogenic granites indicate that almost all KGB samples are post-orogenic, A-type granites (Figure 9b). This result shows that the section formed in an extensional environment and a post-collision setting; thus, the granites differed significantly from those granites related to rift and continental uplift (Figure 9c). In addition, the A-type granite in the KGB also falls into the post-orogenic (PA) field (Figure 9d); thus, it differs from anorogenic granites. In summary, the results suggest that the A_2-type granites in the Sabei, Huangyangshan, and Sujiquan plutons of the eastern KGB formed in an extensional environment and a post-collision geotectonic setting at the end of the orogenic event at around 320–315 Ma.

In accordance with the different granites observed in the easternmost and westernmost KGB, the latest report suggests that the area was not an extensional environment in the late Carboniferous but was in transition from compression to extension. The western KGB experienced compression while the eastern KGB underwent extension during the Late Carboniferous (Wang et al., 2025), These discrete structures imply a high probability of the proposed conditions (Figures 9a,c,d).

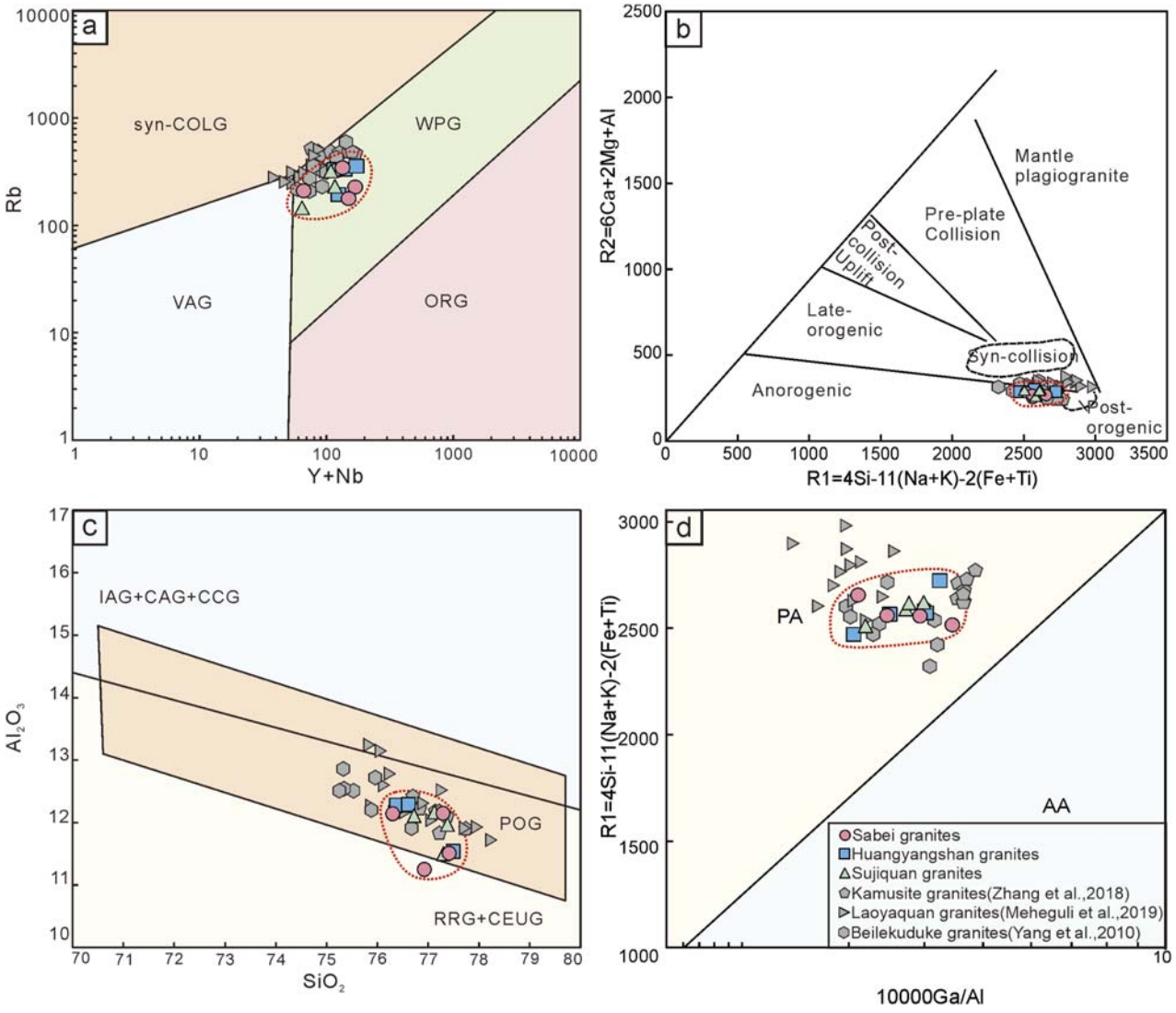

FIGURE 9
(a) Rb vs. Y + Nb (from Pearce et al., 1984); **(b)** R2 vs. R1 (from Batchelor and Bowden, 1985); **(c)** Al_2O_3 vs. SiO_2 (from Harris et al., 1986); and **(d)** R1 vs. 10000Ga/Al (from Hong et al., 1995). RRG, rift-related granitoid; CEUG, continental epeirogenic uplift granitoid; POG, post-orogenic granitoid; IAG, island arc granitoid; CAG, continental arc granitoid; CCG, continental collision granitoid; VAG, volcanic-arc granites; Syn-COLG, syn-collisional granites; WPG, within-plate granites; ORG, ocean-ridge granites; Post-COLG, post-collisional granites; PA, post-orogenic granites; AA, anorogenic granites.

6.4 Magma mixing under crustal growth

Magma reservoirs serve as critical loci for analyzing upper crustal magmatic processes. Crystal mush—formed through multiple magma intrusions (Bachmann and Bergantz, 2004; Coleman et al., 2004; Glazner et al., 2004; Lipman, 2007; Miller et al., 2009; Lipman and Bachmann, 2015; Blundy and Annen, 2016; Ma et al., 2020; Zhang et al., 2022)—exhibits high crystallinity, elevated viscosity, and limited mobility, inhibiting convection, fractionation, and mixing (Bachmann and Bergantz, 2004; Bachmann and Huber, 2016; Ma et al., 2020). However, large-scale upwelling of mantle-derived mafic magma thermally rejuvenates viscous crystal-rich mush, elevating temperatures, reducing viscosity, increasing melt fraction, and decreasing crystallinity. Injection of this high-temperature mafic magma into cooler silicic host magma facilitates mixing, driving rapid compositional hybridization. This process can transform mafic melts into intermediate compositions (e.g., basaltic-andesite to diorite) through combined assimilation and fractional crystallization (Cooper and Kent, 2014; Miller, 2016; Rubin et al., 2017; Jackson et al., 2018; Wilson et al., 2021). The relatively low solidus temperature of dioritic magma promotes early crystallization, forming cumulate textures. Chemical exchange between MMEs and host granite diminishes as magmas cool (Wang, 2000). During flow emplacement, large enclave swarms may fragment into smaller MMEs (Figure 2a). Buoyancy-driven ascent of crystal-rich mush through overlying strata may culminate in volcanic eruptions (Annen, 2009; Spera et al., 2016; Ma et al., 2020) (Figures 10, 11).

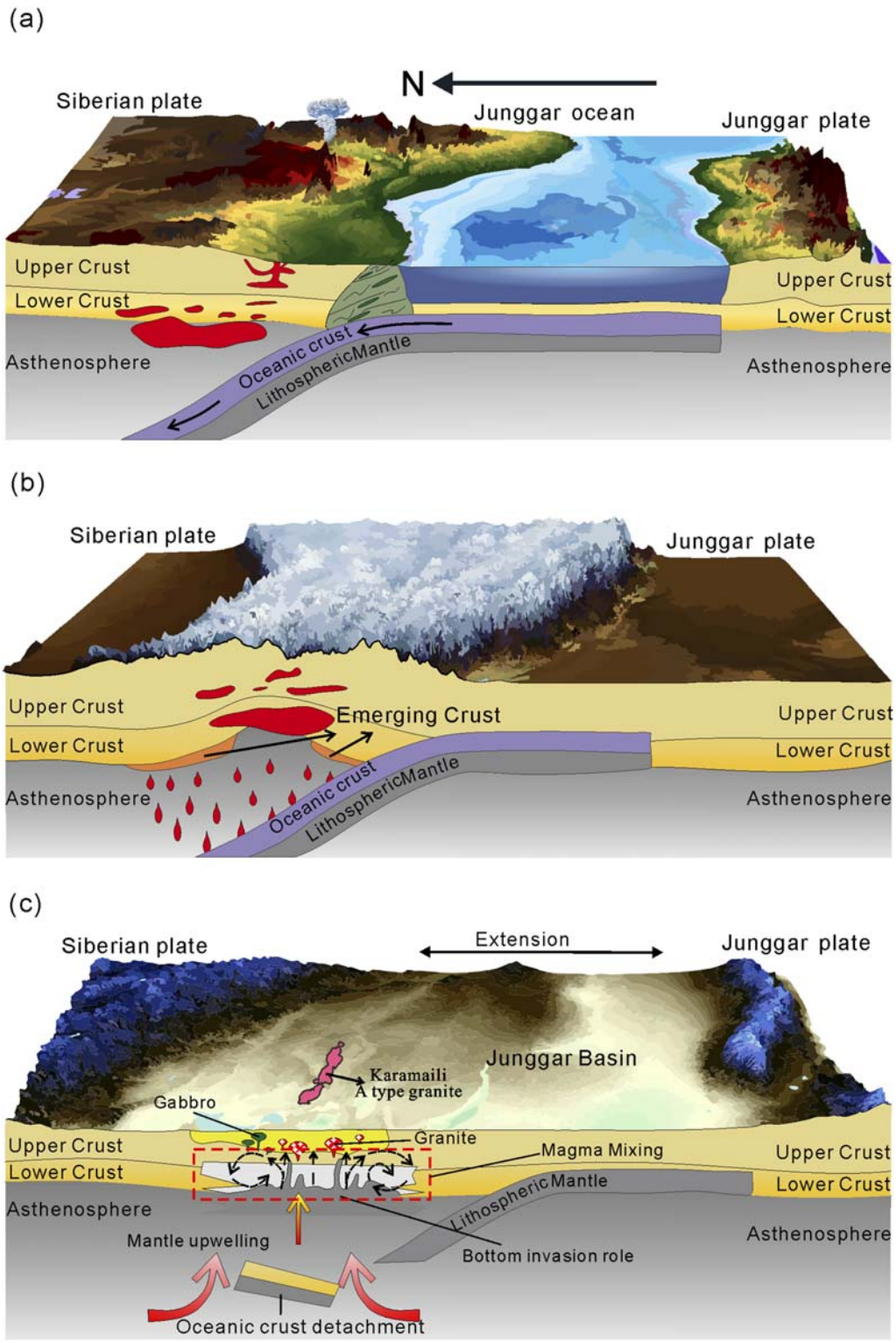

FIGURE 10
Tectonic evolution model map of the Junggar plate (modified after Zhang et al. (2020)). **(a)** Late early Devonian - early middle devonian plate subduction period. **(b)** Early Carboniferous synclinical period. **(c)** Late Carboniferous -Permian extensional period.

As magma ascends from the magma reservoir toward the Earth's surface, mineral crystallization and fractionation can significantly alter its composition (Elburg, 1996). The MMEs have zircon U-Pb ages consistent with those of the host granites; however, compositional differences in major and trace elements are observed. As shown in Figure 5i, the linear relationship between MMEs and the host granite is consistent with the magma evolutionary trends (Langmuir et al., 1978), suggesting that the MMEs and host granite

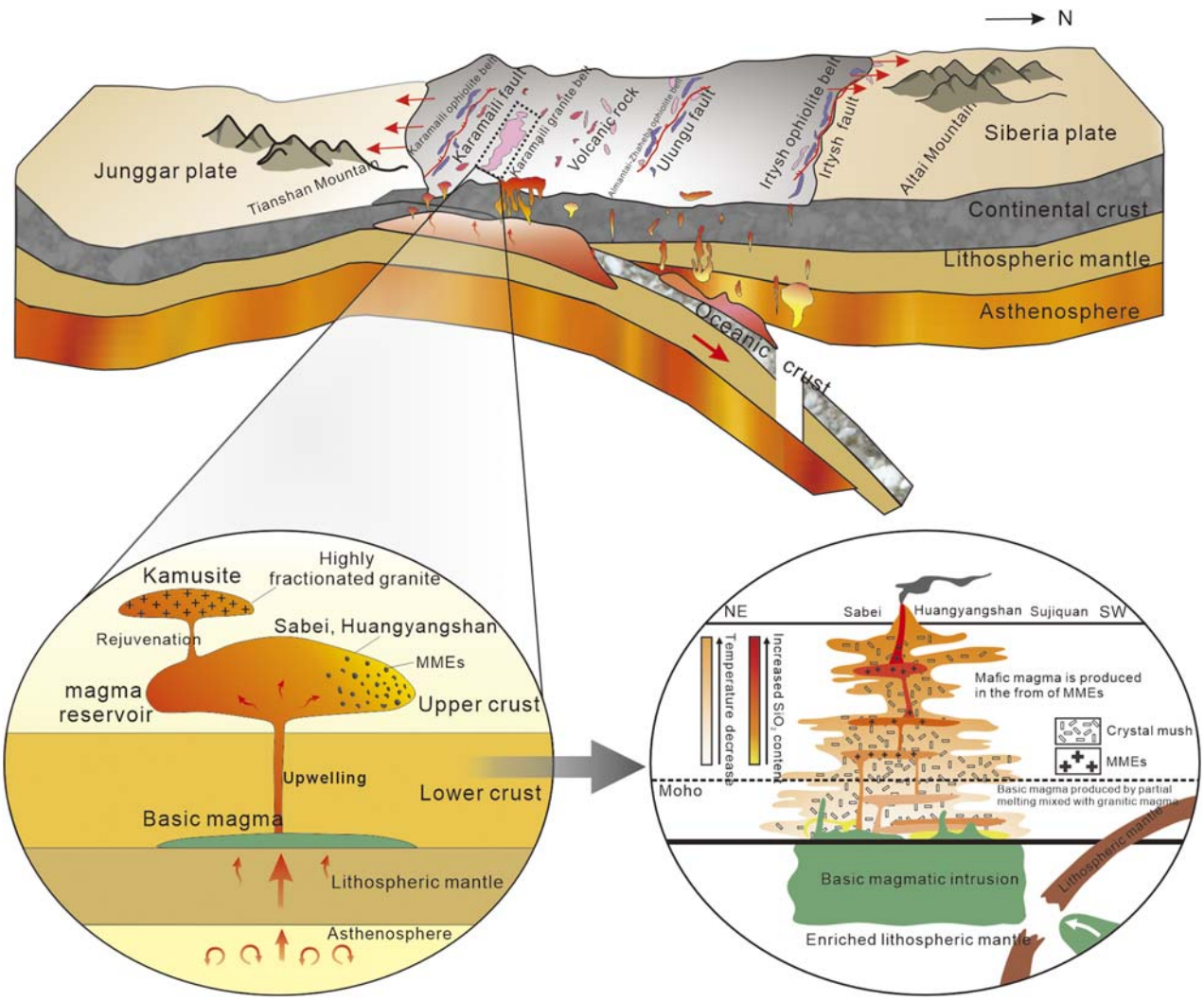

FIGURE 11
Magma mixing model map of the Karamaili (modified after Cashman et al. (2017); Wang et al. (2025)).

are products of magma mixing rather than crystallization and fractionation. The mafic enclaves in the Sabei Pluton are dioritic rather than gabbroic. The $Mg^{\#}$ value is higher than that of the host granite; however, the highest value 55.3 is smaller than the average value obtained for the primitive mantle ($Mg^{\#}$>70) (Bloomer and Hawkins, 1987). The $Mg^{\#}$ value is commonly used to indicate the degree of partial mantle melting. The mantle peridotite with a high $Mg^{\#}$ value (>90) may have undergone a higher degree of partial melting, whereas the $Mg^{\#}$ value of the Sabei MMEs (maximum value of 55.3) suggests that the mantle-derived basic magma did not undergo extensive partial melting but was mixed with granitic magma during its ascent, leading to a simultaneous decrease in the $Mg^{\#}$ value and SiO_2 content (Figures 8b, 12). In addition, the MMEs in Sabei exhibit a mantle-crust evolutionary trend, which is characterized by a decreasing Sr content and an increasing Rb content which is not observed in the host granite. Unlike the Sabei granite, the MMEs have high Mg and Fe contents but low Si and Na contents. Moreover, the zircon U-Pb age is consistent with that of the host granite, recording syn-ascension mixing of mantle-derived mafic and crustal felsic magmas prior to Late Carboniferous emplacement.

The CAOB experienced Phanerozoic juvenile crustal growth, with estimates exceeding 50% (Şengör et al., 1993). The zircon εHf (t) value and whole rock Nd isotope εNd(t) of the granites in the East Junggar are significantly higher than zero, indicating substantial crustal growth in the region during the Late Paleozoic (Su et al., 2007; Tang et al., 2007; Yang et al., 2008; Wang et al., 2023). The zircon εHf (t) values of the granites in the KGB are high, ranging from +10.5 to +14.7, which is close to the value for the depleted mantle (Han et al., 1997; Chen and Arakawa, 2005; Chen et al., 2010). This result suggests that the source is juvenile crust (Wu et al., 2007; Wang and Hou, 2018). In contrast, the granites of Western Junggar are characterized by lower εHf(t) values (Tang et al., 2008; Geng et al., 2009). The whole-rock εNd (t) values are +4.0 to +4.5 (as are the values obtained for the Sabei and Sujiquan plutons); all values are positive (Figures 13a,b), indicating they may have been formed by the remelting of new

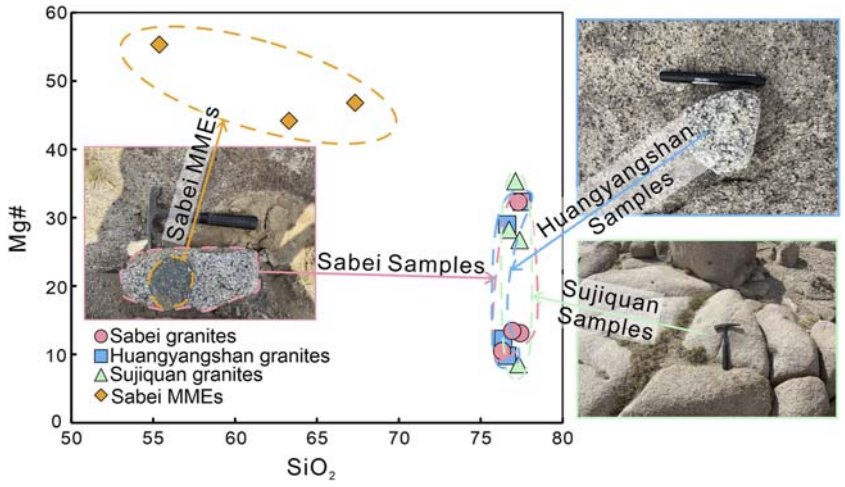

FIGURE 12
Mg# vs. SiO_2 diagrams and field photographs of MMEs and their host granitoids. Mg# is calculated using 100 × MgO/(MgO + TFeO). Composition of metabasaltic and eclogite experimental melts and AFC curves are after Rapp and Brucewatson (1995), Rapp et al. (1999), and Wang et al. (2006).

crustal materials or the differentiation of mantle-derived magma (Whalen et al., 1987; Han et al., 1997; Wu et al., 2003; Bonin, 2007). The Sm/Nd-εNd(t) diagram (Figure 13a) indicates that the granites in the KGB are strongly influenced by continental contamination. The Sabei MMEs show a linear relationship with the host rock, reflecting the evolution of basic and siliceous magma. Additionally, the whole-rock Nd model age (T_{DM2}) of the KGB is in the range 600–650 Ma, suggesting its source area was the Neoproterozoic juvenile lower crust (Wang et al., 2009), which is consistent with the zircon Hf model age (T_{DM2}) (Zhang et al., 2021). The Karamaili granite formed by remelting of earlier-accreted juvenile crustal material, which originated from depleted mantle sources during prior subduction (Jahn et al., 2000). Its emplacement reflects crustal reworking rather than primary growth. Crucially, "vertical crustal growth" refers to magmatic underplating at the crust-mantle boundary (Rudnick and Taylor, 1987), where new mantle-derived melts crystallize beneath pre-existing crust, increasing net crustal thickness and mass. During ascent, these juvenile magmas assimilated upper-crustal components (e.g., metasedimentary rocks), evidenced by inherited Proterozoic zircon cores and elevated $\delta^{18}O$ values. Concurrent magma mixing with mantle-derived melts generated MMEs, supported by disequilibrium textures and Hf-Nd isotope decoupling (Kemp et al., 2009). Spatial variations in the KGB manifest this process: shallow emplacement in the eastern Sabei and Sujiquan plutons preserved abundant MMEs due to limited residence time, whereas prolonged fractionation in western Kamusite pluton formed highly differentiated granites.

In summary, the oceanic crust broke off and caused unbalanced delamination during the subduction at the end of the Late Carboniferous (Zhang et al., 2021), causing the partial melting of large amounts of mantle-derived materials. This event led to underplating at the bottom of the lower crust, triggering upwelling of the basic magma and resulting in the recharge and strong activation of the siliceous magmatic reservoir in the upper crust. Small amounts of basic magma caused the strong activation of the Kamusite and Laoyaquan plutons in the western part of the KGB. Thus, the high-silica melt was extracted from reactivated crystal mush from the high-silicon melt, forming highly differentiated granites with minimal magma mixing signatures. A large amount of basic magma was exchanged with the magma of the Sabei, Huangyangshan, and Sujiquan plutons in the eastern section. Many MMEs were formed by the mixing of basic and siliceous magma, which is manifesting as local-scale magma mixing. A slightly later gabbro pluton (311–307 Ma) of non-ophiolitic origin in the KGB confirms the presence of basic magma in the Late Carboniferous (Wang et al., 2025). Additionally, a large number of diorite and gabbro veins formed in the Sujiquan and Huangyangshan granites in the eastern KGB, differing from the felsic veins that developed only in the Kamusite and Laoyaquan granites of the western KGB. Thus, the supply of basic magma was the dominant factor determining the final occurrence of siliceous magma, which implies both local-scale (mixing) and regional-scale (underplating) impacts of mafic magmatism. In other words, the geochemical linear evolution of the MMEs in the Sabei pluton shows that the injection of basic magma into siliceous magma is a continuous and multi-stage magmatic mixing (Figure 5a–i).

7 Conclusion

1. Zircon U-Pb ages of 315.9 ± 2.4 Ma, 316.1 ± 2.2 Ma, and 319.4 ± 2.0 Ma were obtained for the Sabei monzogranite, Huangyangshan biotite syenogranite, and Sujiquan biotite granite in the eastern KGB, intrusion during the Late Carboniferous. The 313.9 ± 3.5 Ma obtained for the Sabei MMEs is nearly identical to the age of the host granite.
2. The granites comprising the Sabei, Huangyangshan, and Sujiquan plutons are A_2-type granites characterized by high contents of silica, potassium-richness, high-alkali content, and strongly negative Eu anomalies. These granites formed in post-collisional extensional environments, indicating the vertical growth of the juvenile crust during the Late Paleozoic.

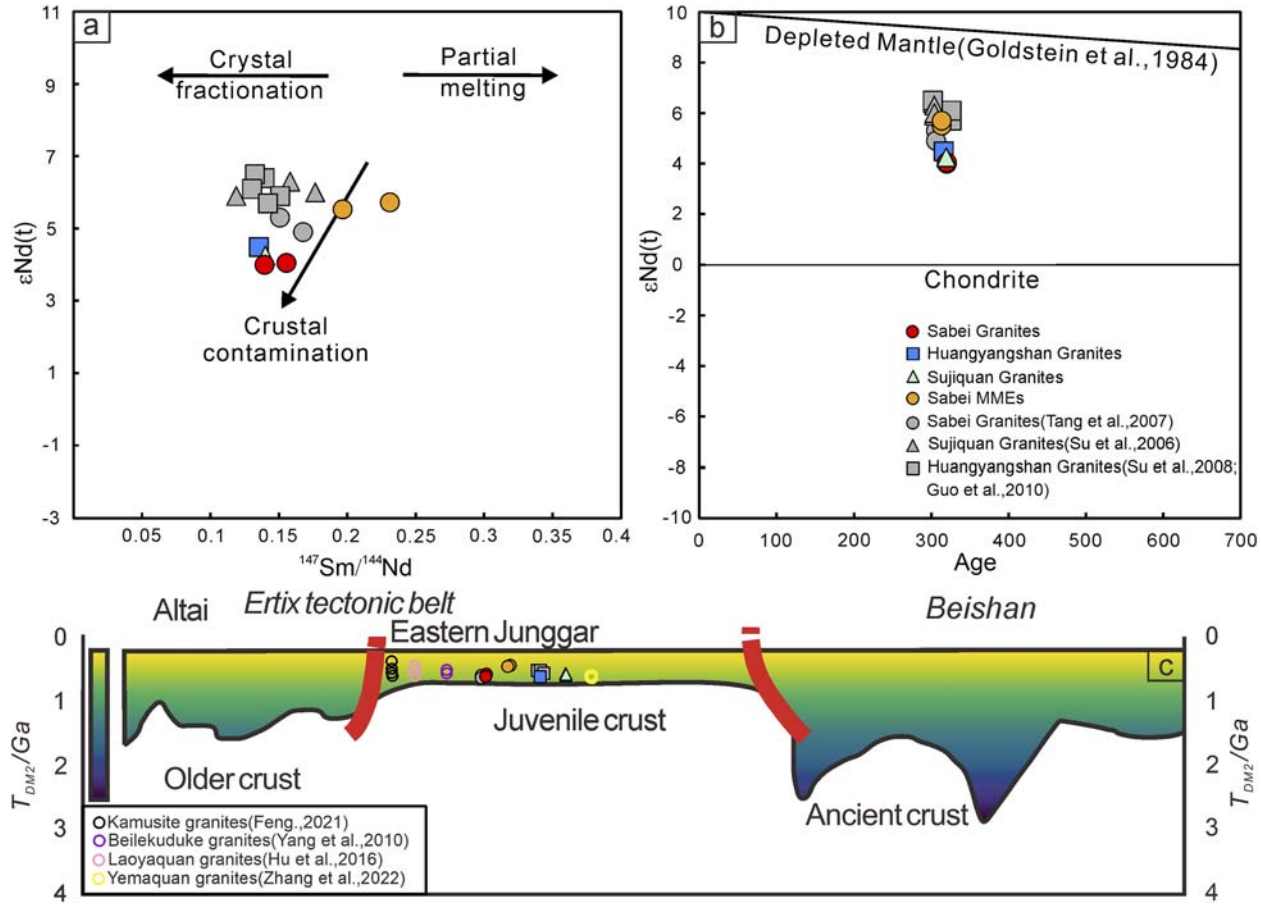

FIGURE 13
(a) εNd(t) vs. Sm/Nd (Dilek et al., 2008); **(b)** εNd(t) vs. Age (Goldstein et al., 1984); **(c)** Nd-mode age profile of the Altai-Junggar-Beishan granite (modified after Wang and Hou (2018)).

3. The abundant MMEs in the granite of the Sabei pluton, which are dioritic enclaves, suggest magma mixing. They are the product of basic magma injected into felsic magma.
4. Spatial differences were observed in the evolution of the KGB. The western pluton was activated by basic magma, resulting in the formation of highly differentiated granites, such as the Kamusite granite. In contrast, the eastern plutons received large amounts of basic magma, forming A_2-type granites rich in dioritic enclaves, such as the Sabei granite.
5. The formation of the Karamaili A-type granitic belt is associated with the vertical accretion of the late Paleozoic juvenile crust.

Data availability statement

The original contributions presented in the study are included in the article/supplementary material, further inquiries can be directed to the corresponding author.

Ethics statement

Written informed consent was obtained from the individual(s), and minor(s)' legal guardian/next of kin, for the publication of any potentially identifiable images or data included in this article.

Author contributions

YS: Writing – original draft, Software, Supervision, Methodology, Data curation, Writing – review and editing, Investigation, Validation. BZ: Investigation, Supervision, Writing – review and editing, Project administration, Methodology, Resources. YuY: Writing – review and editing, Supervision, Data curation, Funding acquisition, Project administration. XZ: Supervision, Conceptualization, Writing – review and editing, Software, Data curation. YaY: Investigation, Writing – review and editing, Conceptualization, Supervision, Validation. YW: Validation, Supervision, Software, Writing – review and editing.

Funding

The author(s) declare that financial support was received for the research and/or publication of this article. This work was supported by the National Key Research and Development Program (Grant No. 2022YFC3003700), Key R&D Program of Xinjiang Uygur Autonomous Region (Grant No. 2024B01015), and the Key Research and Development Program of Xinjiang Production and Construction Corps (Grant No. 2024AB077).

Conflict of interest

The authors declare that the research was conducted in the absence of any commercial or financial relationships that could be construed as a potential conflict of interest.

Generative AI statement

The author(s) declare that no Generative AI was used in the creation of this manuscript.

Any alternative text (alt text) provided alongside figures in this article has been generated by Frontiers with the support of artificial intelligence and reasonable efforts have been made to ensure accuracy, including review by the authors wherever possible. If you identify any issues, please contact us.

Publisher's note

References

Alberto, E., and Patino, D. (1997). Generation of metaluminous A-type granites by low-pressure melting of calc-alkaline granitoids. *Geology* 25 (8), 743. doi:10.1130/0091-7613(1997)025<0743:gomatg>2.3.co;2

Annen, C. (2009). From plutons to magma chambers: thermal constraints on the accumulation of eruptible silicic magma in the upper crust. *Earth Planet. Sci. Lett.* 284 (3), 409–416. doi:10.1016/j.epsl.2009.05.006

Bachmann, O., and Bergantz, G. W. (2004). On the origin of crystal-poor rhyolites: extracted from batholithic crystal mushes. *J. Petrology* 45 (8), 1565–1582. doi:10.1093/petrology/egh019

Bachmann, O., and Huber, C. (2016). Silicic magma reservoirs in the Earth's crust. *Am. Mineralogist* 101 (11), 2377–2404. doi:10.2138/am-2016-5675

Barbarin, B. (1988). Field evidence for successive mixing and mingling between the Piolard Diorite and the Saint-Julien-la-vêtre Monzogranite (Nord–Forez, Massif Central, France). *Can. J. Earth Sci.* 25 (1), 49–59. doi:10.1139/e88-005

Barbarin, B. (2005). Mafic magmatic enclaves and mafic rocks associated with some granitoids of the central Sierra Nevada batholith, California: nature, origin, and relations with the hosts. *Lithos* 80 (1-4), 155–177. doi:10.1016/j.lithos.2004.05.010

Barbarin, B., and Didier, J. (1992). Genesis and evolution of mafic microgranular enclaves through various types of interaction between coexisting felsic and mafic magmas. *Trans. R. Soc. Edinb. Earth Sci.* 83 (1-2), 145–153. doi:10.1017/s0263593300007835

Batchelor, R. A., and Bowden, P. (1985). Petrogenetic interpretation of granitoid rock series using multicationic parameters. *Chem. Geol.* 48 (1), 43–55. doi:10.1016/0009-2541(85)90034-8

Baxter, S., and Feely, M. (2002). Magma mixing and mingling textures in granitoids: examples from the Galway Granite, Connemara, Ireland. *Mineralogy Petrology* 76 (1-2), 63–74. doi:10.1007/s007100200032

Belousova, E., Griffin, W., O'Reilly, S. Y., and Fisher, N. (2002). Igneous zircon: trace element composition as an indicator of source rock type. *Contributions Mineralogy Petrology* 143 (5), 602–622. doi:10.1007/s00410-002-0364-7

Bloomer, S. H., and Hawkins, J. W. (1987). Petrology and geochemistry of boninite series volcanic rocks from the Mariana trench. *Contributions Mineralogy Petrology* 97 (3), 361–377. doi:10.1007/bf00371999

Blundy, J. D., and Annen, C. J. (2016). Crustal magmatic systems from the perspective of heat transfer. *Elements* 12 (2), 115–120. doi:10.2113/gselements.12.2.115

Bonin, B. (2007). A-type granites and related rocks: evolution of a concept, problems and prospects. *LITHOS* 97 (1), 1–29. doi:10.1016/j.lithos.2006.12.007

Brown, G. C., and Fyfe, W. S. (1970). The production of granitic melts during ultrametamorphism. *Contributions Mineralogy Petrology* 28 (4), 310–318. doi:10.1007/bf00388953

Cai, K., Sun, M., Yuan, C., Xiao, W., Zhao, G., Long, X., et al. (2012). Carboniferous mantle-derived felsic intrusion in the Chinese Altai, NW China: implications for geodynamic change of the accretionary orogenic belt. *Gondwana Res.* 22 (2), 681–698. doi:10.1016/j.gr.2011.11.008

Cashman, K. V., Sparks, R. S. J., and Blundy, J. D. (2017). Vertically extensive and unstable magmatic systems: a unified view of igneous processes. *Science* 355 (6331), 3055. doi:10.1126/science.aag3055

Champion, D. C., and Bultitude, R. J. (2013). The geochemical and SrNd isotopic characteristics of Paleozoic fractionated S-types granites of north Queensland: implications for S-type granite petrogenesis. *Lithos* 162–163, 37–56. doi:10.1016/j.lithos.2012.11.022

Chappell, B. W., and White, A. J. R. (1991). Restite enclaves and the restite model. Enclaves and granite petrology. *Enclaves Granite Petrology* 37 (4), 375–381.

Chappell, B. W., and Wyborn, D. (2012). Origin of enclaves in S-type granites of the Lachlan Fold Belt. *Lithos* 154, 235–247. doi:10.1016/j.lithos.2012.07.012

Chappell, B. W., White, A. J. R., and Wyborn, D. (1987). The importance of residual source material (Restite) in granite petrogenesis. *J. Petrology* 28 (6), 1111–1138. doi:10.1093/petrology/28.6.1111

Chen, B., and Arakawa, Y. (2005). Elemental and Nd-Sr isotopic geochemistry of granitoids from the West Junggar foldbelt (NW China), with implications for Phanerozoic continental growth. *Geochimica Cosmochimica Acta* 69 (5), 1307–1320. doi:10.1016/j.gca.2004.09.019

Chen, B., and Jahn, B.-M. (2004). Genesis of post-collisional granitoids and basement nature of the Junggar Terrane, NW China: Nd–Sr isotope and trace element evidence. *J. Asian Earth Sci.* 23 (5), 691–703. doi:10.1016/s1367-9120(03)00118-4

Chen, J., Han, B., and Zhang, L. (2010). Geochemistry,Sr-Nd isotopes and tectonic implications of two generations of late Paleozoic plutons in northern West Junggar,Northwest China. *Acta Petrol. Sin.* 26 (8), 2317–2335.

Coleman, D., Gray, W., and Glazner, A. (2004). Rethinking the emplacement and evolution of zoned plutons: geochronologic evidence for incremental assembly of the Tuolumne Intrusive Suite, California. *Geology* 32 (5), 433–436. doi:10.1130/g20220.1

Cooper, K. M., and Kent, A. J. R. (2014). Erratum: corrigendum: rapid remobilization of magmatic crystals kept in cold storage. *Nature* 508 (7497), 554. doi:10.1038/nature13280

Dahlquist, J. A. (2002). Mafic microgranular enclaves: early segregation from metaluminous magma (Sierra de Chepes), Pampean Ranges, NW Argentina. *J. S. Am. Earth Sci.* 15 (6), 643–655. doi:10.1016/s0895-9811(02)00112-8

Dilek, Y., Furnes, H., and Shallo, M. (2008). Geochemistry of the Jurassic Mirdita Ophiolite (Albania) and the MORB to SSZ evolution of a marginal basin oceanic crust. *LITHOS* 100 (1), 174–209. doi:10.1016/j.lithos.2007.06.026

Donaire, T., Pascual, E., Pin, C., and Duthou, J.-L. (2005). Microgranular enclaves as evidence of rapid cooling in granitoid rocks: the case of the Los Pedroches granodiorite, Iberian Massif, Spain. *Contributions Mineralogy Petrology* 149 (3), 247–265. doi:10.1007/s00410-005-0652-0

Eby, G. N. (1992). Chemical subdivision of the A-type granitoids:petrogenetic and tectonic implications. *Geology* 20 (7), 641–644. doi:10.1130/0091-7613(1992)020<0641:csotat>2.3.co;2

Elburg, M. A. (1996). Evidence of isotopic equilibration between microgranitoid enclaves and host granodiorite, Warburton Granodiorite, Lachlan Fold Belt, Australia. *LITHOS* 38 (1), 1–22. doi:10.1016/0024-4937(96)00003-5

Gan, L., Tang, H. F., and Han, Y. J. (2010). Geochronology and geochemical characteristics of the Yemaquan granitic pluton in East Junggar, Xinjiang. *Acta Petrol. Sin.* 26 (08), 2374–2388.

Geng, H., Sun, M., Yuan, C., Xiao, W., Xian, W., Zhao, G., et al. (2009). Geochemical, Sr-Nd and U-Pb-Hf isotopic studies of late Carboniferous magmatism in the West Junggar, Xinjiang: implications for ridge subduction. *Chem. Geol.* 266, 364–389. doi:10.1016/j.chemgeo.2009.07.001

Glazner, A. F., Bartley, J. M., Coleman, D. S., Gray, W., and Taylor, R. Z. (2004). Are plutons assembled over millions of years by amalgamation from small magma chambers? *GSA Today* 14, 4–11. doi:10.1130/1052-5173(2004)014<0004:apaomo>2.0.co;2

Goldstein, S. L., O'Nions, R. K., and Hamilton, P. J. (1984). A Sm-Nd isotopic study of atmospheric dusts and particulates from major river systems. *Earth Planet. Sci. Lett.* 70 (2), 221–236. doi:10.1016/0012-821x(84)90007-4

Gu, X., Zhang, Y., Ge, Z., Chen, W., Xu, J., Huang, G., et al. (2020). The orogenic Au mineralization system and regional tectonic evolution in the Kalamaili area, East Junggar, Xinjiang. *Earth Sci. Front.* 27 (02), 254–275. doi:10.13745/j.esf.sf.2020.3.21

Hamilton, P. J., O'Nions, R. K., Bridgwater, D., and Nutman, A. (1983). Sm-Nd studies of Archaean meta sediments and metavolcanics from West Greenland and their implications for the Earth's early history. *Earth Planet. Sci. Lett.* 62 (2), 263–272. doi:10.1016/0012-821x(83)90089-4

Han, B., Wang, S., Jahn, B. M., Hong, D., Kagami, H., and Sun, Y. (1997). Depleted-mantle source for the Ulungur River A-type granites from North Xinjiang, China: geochemistry and Nd-Sr isotopic evidence, and implications for Phanerozoic crustal growth. *Chem. Geol.* 138 (3), 135–159. doi:10.1016/s0009-2541(97)00003-x

Han, B., Ji, J., Song, B., Chen, L., and Zhang, L. (2006). Late Paleozoic vertical growth of continental crust around the Junggar Basin, Xinjiang, China (Part I):Timing of post-collisional plutonism. *Acta Petrol. Sin.* 22 (05), 1077–1086.

Han, Y. J., Tang, H. F., and Gan, L. (2012). Zircon U-Pb ages and geochemical characteristics of the laoyaquan A-type granites in East Junggar, North Xinjiang, China. *Acta Mineral. Sin.* 32 (02), 193–199. doi:10.16461/j.cnki.1000-4734.2012.02.020

Harris, N., Pearce, J., and Tindle, A. G. (1986). Geochemical characteristics of collision-zone magmatism. *Geol. Soc. Am. Bull.* 19 (1), 67–81. doi:10.1144/gsl.sp.1986.019.01.04

Hong, D. W., Wang, S. G., Han, B., and Jin, M. Y. (1995). Tectonic-environmental classification of alkaline granites and their identifying markers. *Sci. Sin.* 25 (04), 418–426.

Hoskin, P. W. O., and Ireland, T. R. (2000). Rare Earth element chemistry of zircon and its use as a provenance indicator. *Geology* 28 (7), 627–630. doi:10.1130/0091-7613(2000)028<0627:reecoz>2.3.co;2

Jackson, M. D., Blundy, J., and Sparks, R. S. J. (2018). Chemical differentiation, cold storage and remobilization of magma in the Earth's crust. *Nature* 564 (7736), 405–409. doi:10.1038/s41586-018-0746-2

Jahn, B. M., Wu, F., and Chen, B. (2000). Massive granitoid generation in Central Asia: and isotope evidence and implication for continental growth in the Phanerozoic. *Episodes* 23 (2), 82–92. doi:10.18814/epiiugs/2000/v23i2/001

Jian, P., Liu, D., and Sun, X. (2003). SHRIMP dating of carbpniferous Jinshajiang ophiolite in Western Yunnan and Sichuan: geochronological constraints on the evolution of the paleo-tethys Oceanic crust. *Acta Geol. Sin.* 77 (4), 969–1001.

Kemp, A. I. S., Hawkesworth, C. J., Collins, W. J., Gray, C. M., and Blevin, P. L. (2009). Isotopic evidence for rapid continental growth in an extensional accretionary orogen: the Tasmanides, eastern Australia. *Earth Planet. Sci. Lett.* 284 (3), 455–466. doi:10.1016/j.epsl.2009.05.011

Kempton, P. D., Dungan, M. A., and Blanchard, D. P. (1987). Petrology and geochemistry of xenolith-bearing alkalic basalts from the Geronimo Volcanic Field, southeast Arizona; evidence for polybaric fractionation and implications for mantle heterogeneity. *Am. J. Sci.*, 347–370. doi:10.1130/spe215-p347

King, P. L., White, A. J. R., Chappell, B. W., and Allen, C. M. (1997). Characterization and origin of aluminous A-type granites from the lachlan fold Belt, Southeastern Australia. *J. Petrology* 38 (3), 371–391. doi:10.1093/petroj/38.3.371

Kröner, A., Alexeiev, D. V., Kovach, V. P., Rojas-Agramonte, Y., Tretyakov, A. A., Mikolaichuk, A., et al. (2017). Zircon ages, geochemistry and Nd isotopic systematics for the Palaeoproterozoic 2.3–1.8 Ga Kuilyu complex, East Kyrgyzstan–the oldest continental basement fragment in the Tianshan orogenic belt. *J. Asian Earth Sci.* 135, 122–135. doi:10.1016/j.jseaes.2016.12.022

Kumar, S., and Rino, V. (2006). Mineralogy and geochemistry of microgranular enclaves in Palaeoproterozoic Malanjkhand granitoids, central India: evidence of magma mixing, mingling, and chemical equilibration. *Contributions Mineralogy Petrology* 152 (5), 591–609. doi:10.1007/s00410-006-0122-3

Langmuir, C. H., Vocke, R. D., Hanson, G. N., and Hart, S. R. (1978). A general mixing equation with applications to Icelandic basalts. *Earth Planet. Sci. Lett.* 37 (3), 380–392. doi:10.1016/0012-821x(78)90053-5

Lei, C., Wu, J., Yin, X., Liu, W., Wang, B., Li, W., et al. (2019). Geochronology, geochemistry and geodynamic significance of Awengcuo composite pluton and its dark microgranular enclaves in the north of Tibet. *Geol. Bull. China* 38 (04), 494–508.

Li, J. Y. (1995). Main characteristics and emplacement processes of the east Junggar Ophiolites, Xinjiang, China. *Acta Petrol. Sin.* 11 (S1), 73–84.

Li, C. (2002). Comment on the Magma Mixing and their research. *Bull. Geol. Sci. Technol.* 49–54.

Li, X., Xu, X., Chen, J., Tang, Z., Zhang, Y., and Sun, X. (2012). Zircon dating and geochemical characteristics of Agashen Obo volcanic rocks in eastern Junggar, Xinjiang. *Geol. Bull. China* 31 (12), 2052–2062.

Li, D., He, D., and Fan, C. (2015). Geochronology and sr-nd-hf isotopic composition of the granites, enclaves, and dikes in the Karamay area, NW China: insights into late Carboniferous crustal growth of West Junggar. *Geosci. Front.* 6 (02), 153–173. doi:10.1016/j.gsf.2013.10.005

Lin, J., Yu, H., Yu, X., Di, Y., and Tian, J. (2007). Zircon SHRIMP U-Pb dating and geological implication of the Sabei alkali-rich granite from Eastern Junggar of Xinjiang, NW China. *Acta Petrol. Sin.* 23 (08), 1876–1884.

Lin, J., Yu, H., Wu, C., Su, W., and Guo, J. (2008). Zircon SHRIMP U-Pb dating and geological implication of the Sabei Tin ore-deposit from Eastern Junggar of Xinjiang, China. *Geol. China* 35 (06), 1197–1205.

Lipman, P. W. (2007). Incremental assembly and prolonged consolidation of Cordilleran magma chambers: evidence from the Southern Rocky Mountain volcanic field. *Geosphere* 3 (1), 42–70. doi:10.1130/ges00061.1

Lipman, P. W., and Bachmann, O. (2015). Ignimbrites to batholiths: integrating perspectives from geological, geophysical, and geochronological data. *Geosphere* 11 (3), 705–743. doi:10.1130/ges01091.1

Liu, J., Yu, H., and Wu, G. (1997). Alkali granites and Tin deposits of the Kalamaili area, Northern Xinjiang. *Mineral. Explor.*

Liu, Y., Gao, S., Hu, Z., Gao, C., Zong, K., and Wang, D. (2010). Continental and Oceanic crust recycling-induced melt-peridotite interactions in the trans-north China orogen: U-Pb dating, Hf isotopes and trace elements in zircons from Mantle xenoliths. *J. Petrology* 51 (1-2), 537–571. doi:10.1093/petrology/egp082

Liu, X., Xiao, W., Xu, J., Castillo, P. R., and Shi, Y. (2017). Geochemical signature and rock associations of ocean ridge-subduction: evidence from the Karamaili Paleo-Asian ophiolite in east Junggar, NW China. *Gondwana Res.* 48 (2017), 34–49. doi:10.1016/j.gr.2017.03.010

Ludwig, K. R. (2003). ISOPLOT 3.0: a geochronological toolkit for Microsoft Excel. *Berkeley Geochronol. Cent. Spec. Publ.* 4, 70.

Ma, C. Q., Zhou, B. W., Gao, K., and Wen, X. (2020). Crystal mush storage, incremental pluton assembly and granitic petrogenesis. *Earth Sci.* 45 (12), 4332–4351. doi:10.3799/dqkx.2020.316

Maas, R., Nicholls, I. A., and Legg, C. (1997). Igneous and metamorphic enclaves in the S-type deddick granodiorite, lachlan fold belt, SE Australia: petrographic, geochemical and Nd-Sr isotopic evidence for crustal melting and magma mixing. *J. Petrology* 38 (7), 815–841. doi:10.1093/petrology/38.7.815

Maniar, P. D., and Piccoli, P. M. (1989). Tectonic discrimination of granitoids. *GeoScienceWorld* 101 (5), 635–643. doi:10.1130/0016-7606(1989)101<0635:tdog>2.3.co;2

Middlemost, E. A. K. (1994). Naming materials in the magma/igneous rock system. *Earth-Science Rev.* 37 (3-4), 215–224. doi:10.1016/0012-8252(94)90029-9

Miller, C. F. (2016). Eruptible magma. *Proc. Natl. Acad. Sci. U. S. A.* 113 (49), 13941–13943. doi:10.1073/pnas.1617105113

Miller, C. F., Furbish, D. J., Walker, B. A., Claiborne, L. L., Koteas, G. C., Bleick, H. A., et al. (2009). Growth of plutons by incremental emplacement of sheets in crystal-rich host: evidence from Miocene intrusions of the Colorado River region, Nevada, USA. *Tectonophysics* 500 (1), 65–77. doi:10.1016/j.tecto.2009.07.011

Mo, X. (2011). Magmatism and evolution of the Tibetan Plateau. *Geol. J. China Univ.* 17 (03), 351–367. doi:10.16108/j.issn1006-7493.2011.03.004

Noyes, H. J., Frey, F. A., and Wones, D. R. (1983). A tale of two plutons: geochemical evidence bearing on the origin and differentiation of the Red Lake and Eagle Peak plutons, central Sierra Nevada, California. *J. Geol.* 91 (5), 487–509. doi:10.1086/628801

O'Hara, M. J. (1977). Geochemical evolution during fractional crystallisation of a periodically refilled magma chamber. *Nature* 266 (5602), 503–507. doi:10.1038/266503a0

Pearce, J. A., Harris, N. B. W., and Tindle, A. G. (1984). Trace element discrimination diagrams for the tectonic interpretation of granitic rocks. *Jour Petrol* 25 (4), 956–983. doi:10.1093/petrology/25.4.956

Peccerillo, A., and Taylor, S. R. (1976). Geochemistry of eocene calc-alkaline volcanic rocks from the Kastamonu area, Northern Turkey. *Contributions Mineralogy Petrology* 58 (1), 63–81. doi:10.1007/bf00384745

Rapp, R. P., and Brucewatson, E. (1995). Dehydration melting of metaba salt at 8–32 kbar: implications for Continental growth and crust-mantle recycling. *J. Petrology* 36 (4), 891–931. doi:10.1093/petrology/36.4.891

Rapp, R. P., Shimizu, N., Norman, M. D., and Applegate, G. S. (1999). Reaction between slab-derived melts and peridotite in the mantle wedge: experimental constraints at 3.8 GPa. *Chem. Geol.* 160 (4), 335–356. doi:10.1016/s0009-2541(99)00106-0

Rubin, A. E., Cooper, K. M., Till, C. B., Kent, A. J. R., Costa, F., Bose, M., et al. (2017). Rapid cooling and cold storage in a silicic magma reservoir recorded in individual crystals. *Science* 356 (6343), 1154–1156. doi:10.1126/science.aam8720

Rudnick, R. L., and Taylor, S. R. (1987). The composition and petrogenesis of the lower crust: a xenolith study. *J. Geophys. Res. Solid Earth* 92 (B13), 13981–14005. doi:10.1029/jb092ib13p13981

Sengör, A. M. C., and Natal'in, B. A. (1996). Turkic-type orogeny and its role in the making of the continental crust. *Annu. Rev. Earth Planet. Sci.* 24 (1), 263–337. doi:10.1146/annurev.earth.24.1.263

Şengör, A. M. C., Natal'in, B. A., and Burtman, V. S. (1993). Evolution of the Altaid tectonic collage and Palaeozoic crustal growth in Eurasia. *Nature* 364, 299–307. doi:10.1038/364299a0

Shellnutt, J. G., Jahn, B. M., and Dostal, J. (2010). Elemental and Sr–Nd isotope geochemistry of microgranular enclaves from peralkaline A-type granitic plutons of the Emeishan large igneous province, SW China. *Lithos* 119 (1-2), 34–46. doi:10.1016/j.lithos.2010.07.011

Shu, L., and Wang, Y. (2003). Late devonian-early Carboniferous Radiolarian fossils from siliceous rocks of the Kelameili ophiolite. *Geol. Rev.* doi:10.16509/j.georeview.2003.04.011

Słaby, E., and Martin, H. (2008). Mafic and felsic magma interaction in granites: the Hercynian Karkonosze Pluton (Sudetes, Bohemian Massif). *J. Petrology* 49 (2), 353–391. doi:10.1093/petrology/egm085

Spera, F. J., Schmidt, J. S., Bohrson, W. A., and Brown, G. A. (2016). Dynamics and thermodynamics of magma mixing: insights from a simple exploratory model. *Am. Mineralogist* 101 (3), 627–643. doi:10.2138/am-2016-5305

Su, Y., Tang, H., Liu, C., Hou, G., and Liang, L. (2006). The determination and a preliminary study of Sujiquan aluminous A-type granite in East Junggar, Xinjiang. *Acta Petrologica Mineralogica* 25 (03), 175–184.

Su, Y., Tang, H., Sylvester, P. J., Liu, C., Cong, F., Hou, G., et al. (2007). Petrogenesis of Karamaili alkaline A-type granites from East Junggar, Xinjiang (NW China) and their relationship with tin mineralization. *Geochem. J.* 41 (5), 341–357. doi:10.2343/geochemj.41.341

Su, Y., Tang, H., and Cong, F. (2008). Zircon U-Pb age and petrogenesis of the Huangyangshan Alkalinegranite body in east Junggar, Xinjiang. *Acta Mineral. Sin.*, 117–126. doi:10.16461/j.cnki.1000-4734.2008.02.002

Sun, S. S., and Mc Donough, W. F. (1989). Chemical and isotopic systematics of oceanic basalts: implications for mantle composition and processes. *Geol. Soc.* 42 (1), 313–345. doi:10.1144/GSL.SP.1989.042.01.19

Tang, H., Su, Y., Liu, C., Hou, G., and Wang, Y. (2007). Zircon U-Pb age of the plagiogranite in Kalamaili belt, northern Xinjiang and its tectonic implications. *Geotect. Metallogenia* 31 (1), 110–117.

Tang, H., Zhao, Z., Huang, R., Han, Y., and Su, Y. (2008). Primary Hf isotopic Study on zircons from the A-type granites in Eastern Junggar of Xinjiang, Northwest China. *Acta Mineral. Sin.* 28 (04), 335–342. doi:10.16461/j.cnki.1000-4734.2008.04.004

Tang, H. F., Su, Y. P., Qiu, H. N., and Han, Y. J. (2009). ^{40}Ar-^{39}Ar age of of tin mineralization in the Beilekuduk tin metallognic belt, East Junggar Xinjiang (NW China). *Acta Petrol. Sin.* 25 (06), 1303–1309.

Wang, T. (2000). Origin of hybrid granitoids and implications for continental dynamics. *Acta Petrol. Sin.* 16 (02), 161–168.

Wang, X. (2017). Some new research progresses and main scientific problems of granitic rocks. *Acta Petrol. Sin.* 33 (05), 1445–1458.

Wang, T., and Hou, Z. (2018). Isotopic mapping and deep material probing (I): revealing the compositional evolution of the lithos phere and crustal growth processes. *Earth Sci. Front.* 25 (06), 1–19. doi:10.13745/j.esf.sf.2018.11.21

Wang, Q., Wyman, D. A., Xu, J. F., Zhao, Z. H., Jian, P., Xiong, X. L., et al. (2006). Petrogenesis of Cretaceous adakitic and shoshonitic igneous rocks in the Luzong area, Anhui Province (eastern China): implications for geodynamics and Cu–Au mineralization. *Lithos* 89 (3-4), 424–446. doi:10.1016/j.lithos.2005.12.010

Wang, T., Jahn, B. M., Kovach, V. P., Tong, Y., Hong, D. W., and Han, B. F. (2009). Nd–Sr isotopic mapping of the Chinese Altai and implications for continental growth in the Central Asian Orogenic Belt. *Lithos* 110 (1-4), 359–372. doi:10.1016/j.lithos.2009.02.001

Wang, Q., Zhao, G., Han, Y., Yao, J., Liu, Q., Guo, Y., et al. (2021). Late Paleozoic tectonic transition in East Junggar, NW China: insights from I-and A-type granitic magmatism in the Karamaili region. *Lithos* 404-405, 106481. doi:10.1016/j.lithos.2021.106481

Wang, T., Li, J., Han, J., Wang, T., Li, Y., and Yuan, B. (2023). Geochemistry, geochronology and Hf isotopic characteristics of rare earth-bearing quartz syenite in eastern Dashuigou, East Kunlun. *Earth Sci. Front.* 30 (4), 283–298. doi:10.13745/j.esf.sf.2023.2.41

Wang, Q., Zhang, B., Ding, J., Zhan, X., Yalikun, Y., Aishan, M., et al. (2025). Origin of the late Carboniferous Karamaili Granite Belt in Eastern Junggar, Northwest China: Zircon U-Pb and trace element constraints. *Int. Geol. Rev.* 67 (2), 166–183. doi:10.1080/00206814.2024.2376324

Whalen, J., Currie, K., and Chappell, B. (1987). A-type granites: geochemical characteristics, discrimination and petrogenesis. *Contributions Mineralogy Petrology* 95 (4), 407–419. doi:10.1007/bf00402202

White, A. J. R., Chappell, B. W., and Doone, W. (1999). Application of the restite model to the Deddick Granodiorite and its enclaves—a reinterpretation of the observations and data of. *J. Petrology* 40 (3), 413–421. doi:10.1093/petroj/40.3.413

Wilson, C. J. N., Cooper, G. F., Chamberlain, K. J., Barker, S. J., Myers, M. L., Illsley, K. F., et al. (2021). No single model for supersized eruptions and their magma bodies. *Nat. Rev. Earth and Environ.* 2 (9), 610–627. doi:10.1038/s43017-021-00191-7

Wright, J. B. (1969). A simple alkalinity ratio and its application to questions of non-orogenic granite genesis. *Geol. Mag.* 106 (4), 370–384. doi:10.1017/s0016756800058222

Wu, F. Y., Jahn, B. M., Wilde, S. A., Lo, C. H., Yui, T. F., Lin, Q., et al. (2003). Highly fractionated I-type granites in NE China (I): geochronology and petrogenesis. *Lithos* 66, 241–273. doi:10.1016/s0024-4937(02)00222-0

Wu, F., Li, X., Zhen, Y., and Gao, S. (2007). Lu-Hf isotopic systematics and their applications in petrology. *Acta Petrol. Sin.* 23 (2), 185–220.

Wyllie, P. J., Cox, K. G., and Biggar, G. M. (1962). The habit of apatite in synthetic systems and igneous rocks. *J. Petrology* 3 (2), 238–243. doi:10.1093/petrology/3.2.238

Xiao, W., and Santosh, M. (2014). The western Central Asian Orogenic Belt: a window to accretionary orogenesis and continental growth. *Gondwana Res.* 25 (4), 1429–1444. doi:10.1016/j.gr.2014.01.008

Xiao, W., Shu, L., and Gao, J. (2008). Continental dynamics of the central Asisn orogenic Belt and its metallogeny. *Xinjiang Geol.* 26 (01), 4–8.

Xiao, Y., Zhang, H., Shi, J. a., Su, B., Sakyi, P. A., Lu, X., et al. (2010). Late Paleozoic magmatic record of East Junggar, NW China and its significance: implication from zircon U–Pb dating and Hf isotope. *Gondwana Res.* 20 (2), 532–542. doi:10.1016/j.gr.2010.12.008

Xiao, W., Song, D., Windley, B. F., Li, J., Han, C., Wan, B., et al. (2019a). Research progresses of the accretionary processes and metallogenesis of the Central Asian Orogenic Belt. *Sci. China Earth Sci.* 49 (10), 1512–1545.

Xiao, W., Yongjiang, L., Zengqian, H., and Shan, L. (2019b). A special issue devoted to the accretionary and collisional tectonics of the Altaids and its metallogeny: preface. *Acta Geol. Sin.* 93 (5). doi:10.1111/1755-6724.14394

Xie, L., Wang, D., Wang, R., Qiu, J., and Chen, X. (2004). Complex zoning texture of phenocryst plagioclase in andesitic rocks of Tancheng area, Shandong Province: record of magma mixing. *Acta Geol. Sin.* 9 (06), 33–41.

Xu, Z., Han, B.-F., Ren, R., Zhou, Y.-Z., Zhang, L., Chen, J.-F., et al. (2011). Ultramafic–mafic mélange, island arc and post-collisional intrusions in the Mayile Mountain, West Junggar, China: implications for Paleozoic intra-oceanic subduction–accretion process. *Lithos* 132, 141–161. doi:10.1016/j.lithos.2011.11.016

Xu, X., Li, R., Chen, J., Ma, Z., Li, Z., Wang, H., et al. (2014). New constrains on the Paleozoic tectonic evolution of the northern Xinjiang area. *Acta Petrol. Sin.* 30 (06), 1521–1534.

Xu, X.-W., Jiang, N., Li, X.-H., Wu, C., Qu, X., Zhou, G., et al. (2015). Spatial–temporal framework for the closure of the Junggar Ocean in central Asia: new SIMS zircon U–Pb ages of the ophiolitic mélange and collisional igneous rocks in the Zhifang area, East Junggar. *J. Asian Earth Sci.* 111, 470–491. doi:10.1016/j.jseaes.2015.06.017

Yang, G., Li, Y., Si, G., Wu, H., Zhang, Y., and Jin, Z. (2008). LA-ICP-MS zircon U-Pb dating of the Kubusunan granodiorite in the Kalamaili area, Eastern Junggar, Xinjiang. *Geol. China.*

Yang, G., Li, Y., Si, G., Wu, H., Zhang, Y., and Jin, Z. (2009). Geochemical characteristics and tin mineralization of the beilekuduke A-type granite in East Junggar. *Geol. Explor.* 45 (05), 530–538.

Zhang, Y. Y., and Guo, Z. J. (2010). New constrains on formation ages of ophiolites in northern Junggar and comparative study on their connection. *Acta Petrol. Sin.* 26 (02), 421–430.

Zhang, J. e., Xiao, W., Han, C., Ao, S., Yuan, C., Sun, M., et al. (2010). Kinematics and age constraints of deformation in a late Carboniferous accretionary complex in Western Junggar, NW China. *Gondwana Res.* 19 (4), 958–974. doi:10.1016/j.gr.2010.10.003

Zhang, Y., Pe-Piper, G., David, W. P., and Guo, Z. (2013). Early Carboniferous collision of the Kalamaili orogenic belt, North Xinjiang, and its implications: evidence from molasse deposits. *Geol. Soc. Am. Bull.* 125, 932–944. doi:10.1130/B30779.1

Zhang, B., Zhan, X., and Daunmu, C. (2018). The Study on petrogeochemistry of kamusite granites in Eastern Junggar and its tectonic significance. *J. Xinjiang Univ. Sci. Ed. Chin. Engl.* 35 (04), 502–512. doi:10.13568/j.cnki.651094.2018.04.017

Zhang, B., Chen, C., Gong, X., Yalikun, Y., and Kaheman, K. (2020). The Kamusite A2-type granites in the Karamaili tectonic belt, Xinjiang (NW China): tracing staged postcollisional delamination in the eastern Junggar. *Geol. Mag.* 158 (4), 723–748.

Zhang, B., Chen, C., Gong, X., Kaheman, K., and Yalikun, Y. (2021). The Kamusite A2-type granites in the Karamaili tectonic belt, Xinjiang (NW China): tracing staged postcollisional delamination in the eastern Junggar. *Geol. Mag.* 158 (4), 723–748. doi:10.1017/S0016756820000813

Zhang, J. H., Zhen, X. X., Sun, J. F., Chen, J. Y., and Yang, J. H. (2022). Dynamic mechanisms of the evolvement of crustal silicic magmas. *Acta Petrol. Sin.* 38 (05), 1481–1498. doi:10.18654/1000-0569/2022.05.13

Zorpi, M. J., Coulon, C., and Orsini, J. B. (1991). Hybridization between felsic and mafic magmas in calc-alkaline granitoids — a case study in northern Sardinia, Italy. *Chem. Geol.* 92 (1), 45–86. doi:10.1016/0009-2541(91)90049-w